

Gas dynamics in massive dense cores in Cygnus-X[★]

T. Csengeri¹, S. Bontemps², N. Schneider¹, F. Motte¹, and S. Dib^{1,3}

¹ Laboratoire AIM, CEA, INSU/CNRS, Université Paris Diderot, IRFU/SaP CEA-Saclay, 91191 Gif-sur-Yvette, France
e-mail: timea.csengeri@cea.fr

² OASU/LAB-UMR5804, CNRS, Université Bordeaux 1, 33270 Floirac, France

³ Astrophysics Group, Imperial College of Science, Technology and Medicine, London SW7 2AZ, UK

Received 13 May 2010 / Accepted 5 November 2010

ABSTRACT

Context. The physical conditions in massive dense cores (MDCs) that form massive stars and clusters, are not well constrained. Few observations have been made to confront the theories. An extensive study has started of the most massive and youngest cores in the Cygnus-X molecular complex, whose first results have uncovered exceptional fragmentation properties in a sample of five cores where individual massive protostars have been recognized.

Aims. We study the kinematic properties of dense gas surrounding massive protostars in these five cores to investigate whether turbulent support plays a major role in stabilizing the whole core against a rapid fragmentation into Jeans-mass objects. The observed kinematics could indicate a high level of dynamics suggesting that the cores are actually not in equilibrium and dynamical processes could be the main driver of the build up of the final stellar masses.

Methods. We present IRAM 30m single-dish (H^{13}CO^+ and HCO^+) data and IRAM Plateau de Bure Interferometer high angular-resolution observations of dense gas tracers (H^{13}CO^+ and H^{13}CN) to reveal the kinematics of molecular gas on scales from 0.03 to 0.1 pc.

Results. Using radiative transfer modeling, we show that the H^{13}CO^+ abundance drops within the envelopes of massive protostars and traces the bulk of material surrounding the protostars instead of their inner envelopes. H^{13}CN shows a better correspondence with the peak of the continuum emission, possibly because of abundance anomalies and specific chemistry in the close vicinity of massive protostars. Analyzing the line-widths, we show that the observed line-dispersion of H^{13}CO^+ on the scale of MDCs is smaller than expected from the quasi-static, turbulent-core model. On large-scales, global organized bulk motions are identified for three of the MDCs. On small-scales, several spectral components are identified in all MDCs showing filamentary structures and intrinsic velocity gradients across the continuum peaks. The dynamics of these flows show diversity across the sample, which we link to the specific fragmentation properties of the MDCs. Altogether this is indicative of different initial conditions in CygX-N3 and -N63 compared to CygX-N12, -N48 and -N53, which may represent different evolutionary stages.

Conclusions. No clear evidence is found of a turbulence-regulated, equilibrium scenario within the sample of MDCs. We propose a picture in which MDCs are not in equilibrium and their dynamics is governed by small-scale converging flows, which may initiate star-formation via their shears. We suggest that dynamical processes are linked to the formation of proto-clusters and high-mass protostars.

Key words. ISM: kinematics and dynamics – radio lines: ISM – molecular data – star: protostars

1. Introduction

Several models have been proposed to explain which processes dominate and form structures within giant molecular complexes, thus determining the origin of star-forming cores and ultimately of stars. On the basis of early scenarios describing the quasi-static evolution of molecular clouds, primarily regulated by the interplay between gravitation and magnetic fields (e.g. Mouschovias & Spitzer 1976; Shu et al. 1987; Mouschovias & Ciolek 1999), the importance of turbulence has now been taken into account (see Mac Low & Klessen 2004; McKee & Ostriker 2007, and references therein). For high-mass star formation, the consideration of the relative importance of these different types of supports against gravity has led to two main alternative views. In the first scenario, molecular clouds are close to being in equilibrium and evolve on long timescales (of the order of several

dynamical crossing times, e.g. Larson 1981; McKee 1999). Since turbulence decays within a dynamical time (e.g. Mac Low et al. 1998; Padoan & Nordlund 1999), it needs to be replenished over such long timescales (e.g. by stellar winds, supernovae explosions, outflows, or other types of feedback; Norman & Silk 1980; McKee 1989) to maintain a quasi-static state. As a result, turbulence can regulate the formation of structures within molecular clouds on large scales, while on small scales isotropic, supersonic turbulence could provide the main support of cores against collapse, thus complementing their thermal pressure (McKee & Tan 2002, 2003). It naturally describes the formation of high-mass stars as a scaled-up scenario of the low-mass, quasi-static star-formation process. Accretion rates of up to $\sim 10^{-3} M_{\odot} \text{ yr}^{-1}$ are reached for these turbulent, massive cores, which is high enough to overcome radiation pressure and enable the protostar to collect a mass higher than 8–10 M_{\odot} . The *turbulence regulated, quasi-static scenario* has fundamental predictions: 1.) the existence of massive cores, which are not yet forming stars (the equivalent of low-mass pre-stellar cores); 2.) a high level of isotropic, supersonic turbulence on the size-scale

[★] The H^{13}CO^+ and H^{13}CN data cubes obtained with the PdBI (associated with Fig. 4) are only available as FITS files at the CDS via anonymous ftp to cdsarc.u-strasbg.fr (130.79.128.5) or via <http://cdsarc.u-strasbg.fr/viz-bin/qcat?J/A+A/527/A135>

of massive cores; 3.) the collapse of massive cores directly into a single (or close binary) massive object. To be more precise, gravitationally unstable density fluctuations are predicted, but with a low number of gravitationally bound fragments within a single core.

Alternatively, clouds and clumps may be unstable, rapidly evolving structures displaying a high level of dynamics (e.g. Vázquez-Semadeni et al. 2002; Klessen & Hennebelle 2010). To summarize, large-scale turbulent flows create structures by shock dissipation and, as shown by numerical simulations, supersonic turbulence fragments the gas efficiently on very short timescales (Padoan et al. 2001; Vázquez-Semadeni et al. 2007). This picture of *gravo-turbulent fragmentation* naturally provides the seeds for star formation by creating gravitationally bound density fluctuations (Klessen et al. 2005; Dib et al. 2007). In hydrodynamic simulations, this results in fragments of mass around the local Jeans mass ($\sim 1 M_{\odot}$), thus it is efficient to produce low-mass fragments, while there is a significant lack of massive ones (Bonnell et al. 2007; Dib et al. 2010b). Bonnell et al. proposed as a solution that seeds may continue to accrete material from regions that were originally not bound to the protostellar envelope. This scenario is therefore introduced as *competitive accretion* (Bonnell et al. 2001; Bonnell & Bate 2006). Massive seeds continue to grow in mass via two mechanisms: by the channelling of material onto the common cluster potential well, and when the relative velocities are too small, the accretion processes are dominated by the tidal field of the protostar itself.

According to Hennebelle & Teyssier (2008), *magnetic fields* can lower the level of fragmentation resulting in only a few more massive objects, which continue to gain mass via channelling of material along the field lines. We note, however, that strong perturbations (that must be seeded in the clumps/cores to allow them to fragment in the presence of magnetic fields) may also naturally be reproduced in the gravo-turbulent fragmentation of magnetically supercritical and nearly critical clouds (Dib et al. 2010a). In the analytic description of Hennebelle & Chabrier (2008) (magnetic field included), the interplay between gravothermal and gravoturbulent fragmentation can naturally reproduce the observed frequency of massive stars – depending on the Mach-number within molecular clouds. The fundamental predictions of the dynamical view are, that 1.) non-isotropic turbulence/velocity fields should be present with dynamical patterns; 2.) a high level of fragmentation is expected with the most massive stars forming at the center of clusters (since they are the most efficient in competing for mass).

We attempt to place observational constraints on the key parameters of current star-formation theories by performing a systematic, high angular-resolution study of massive dense cores (MDCs) in Cygnus-X. (Bontemps et al. 2010, hereafter Paper I) presented 1 mm and 3 mm continuum maps of six IR-quiet MDCs, which were obtained by the Plateau de Bure Interferometer. Twenty-three fragments were detected in a sample of six cores, which challenges the turbulence-regulated, monolithic collapse theory – according to which these cores should be far less fragmented. However, the most compact MDC, CygX-N63, stands out from the picture since it contains only a single, compact object, and could therefore be representative of a single massive protostar with an envelope mass of $\sim 60 M_{\odot}$. In addition, a total of eight fragments are found to be precursors of OB stars with envelope masses ranging from 6–23 M_{\odot} . We found that the level of fragmentation within these MDCs is higher than expected in the quasi-static formation scenario, but lower than predicted by a pure gravo-turbulent scenario. We also compared the mass of the cores with the total

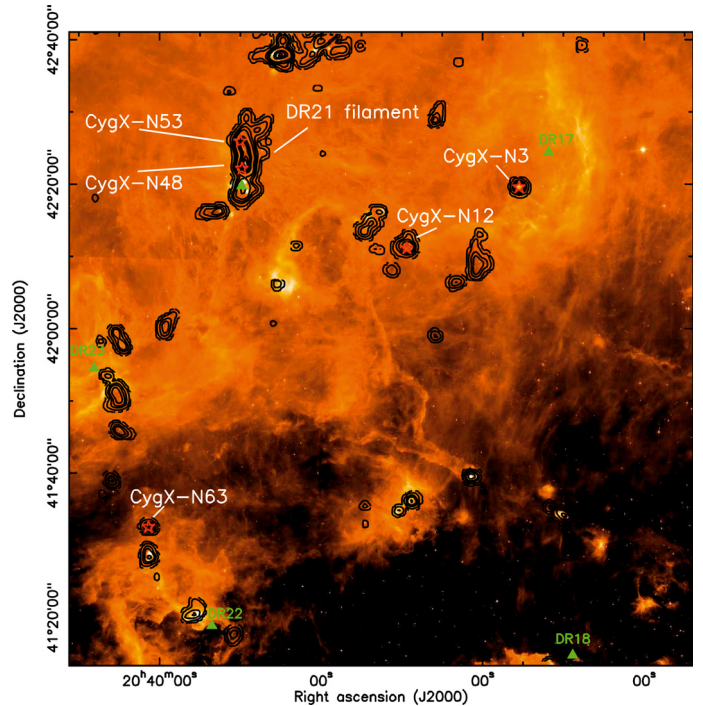


Fig. 1. *Spitzer*/IRAC 8 μm map (Hora et al. 2009) showing a part of Cygnus-X North. Black contours show integrated intensity map of the N_2H^+ ($J = 1-0$) line obtained with the FCRAO (Schneider et al. 2010). Red stars indicate the position of the sample of MDCs. Green triangles indicate the position of HII regions (Downes & Rinehart 1966).

mass contained in the fragments, which is 37%, 58%, and 100% for CygX-N12, CygX-N53, and CygX-N63, respectively. This efficiency of turning the cloud mass into protostars is significantly higher than observed for clusters (Lada & Lada 2003) and predicted for low-mass stars and clusters (Matzner & McKee 2000).

The origin or physical reason for these diverse fragmentation properties is unknown, and can only be elucidated with kinematic studies using molecular lines. Here we present a study of high-density molecular tracers using single-dish observations of $\text{HCO}^+(J = 1-0)$ and $\text{H}^{13}\text{CO}^+(J = 1-0)$ line emission from a sample of MDCs in addition to high angular-resolution, interferometric observations of $\text{H}^{13}\text{CO}^+(J = 1-0)$ and $\text{H}^{13}\text{CN}(J = 1-0)$ lines. These molecules have a high critical density ($>10^4 \text{ cm}^{-3}$, e.g. Bergin & Tafalla 2007) and are known to be tracers of dense gas, hence allow us to probe the dynamics of the gas within MDCs.

2. Source selection and observations

2.1. IR-quiet MDCs in Cygnus-X and sample selection

The source selection is based on the 1.1 mm MAMBO survey of Cygnus-X (Motte et al. 2007), from which we selected the most massive IR-quiet MDCs. All cores are compact with a similar size as nearby low-mass cores ($\sim 0.13 \text{ pc}$), but are both ten times denser (with an average density of $1.9 \times 10^5 \text{ cm}^{-3}$) and 20 times more massive ($\sim 60-200 M_{\odot}$). Therefore one would expect them to be actively forming stars, which is confirmed by the outflow emission detected in SiO. However, the lack of strong mid-IR and free-free emission indicates that they must be in an early stage of their evolution.

Table 1. Observation and data reduction parameters of the interferometric data.

Source	Phase center		H ¹³ CO ⁺			H ¹³ CN		
	RA(J2000)	Dec(J2000)	Beam size [″×″]	PA	Obtained rms [mJy/beam]	Beam size [″×″]	PA	Obtained rms [mJy/beam]
CygX-N3	20:35:34.1	42:20:05.0	3.78 × 3.09	63°	16.3	3.67 × 3.03	53°	11.8
CygX-N12	20:36:57.4	42:11:27.5	4.35 × 3.77	72°	21.2	4.13 × 3.58	65°	14.5
CygX-N48	20:39:01.5	42:22:04.0	4.52 × 3.52	75°	21.0	4.27 × 3.36	71°	13.5
CygX-N53	20:39:03.1	42:25:50.0	4.42 × 3.5	72°	20.3	4.25 × 3.34	69°	14.8
CygX-N63	20:40:05.2	41:32:11.9	4.45 × 3.83	79°	21.3	4.16 × 3.58	66°	14.3

Notes. We give beam-sizes, position angle, and noise levels of H¹³CO⁺ for the combined dataset of PdBI+30 m. For H¹³CN, parameters of the interferometric data are shown.

As shown in Fig. 1, two of the selected cores (CygX-N48 and CygX-N53) are located in the DR21 filament, which is the most massive and densest region of Cygnus-X, and is a well-known region of massive star formation (see e.g. Schneider et al. 2010 and references therein). CygX-N48 corresponds to the submillimeter source DR21(OH)-S, while CygX-N53 is situated close to W75-FIR3 (Chandler et al. 1993). The three other selected MDCs were discovered by the MAMBO survey and are situated in more isolated, but still prominent molecular clumps bright in N₂H⁺ line emission, which equally traces the cold, dense gas. CygX-N3 in the western part is located close to DR17, which is an HII region most probably excited by two OB clusters (clusters #12 and 14 in Le Duigou & Knödlseeder 2002). These clusters are shaping the cloud and CygX-N3 corresponds to the tip of a pillar-like cloud. CygX-N12 is also located in a cometary-shaped cloud, which is probably influenced by the same OB clusters. However, the cloud seems to be less compressed from outside than CygX-N3 (Schneider et al. 2006). Finally, CygX-N63 is placed to the south of DR21 in the DR22-DR23 filament. We adopt a distance of 1.7 kpc for Cygnus-X (Schneider et al. 2006) where 1″ corresponds to 1700 AU.

2.2. Observations

2.2.1. Observations with the IRAM 30 m telescope

OTF maps of the spectral lines of CygX-N3, -N12 and -N63 were compiled on 5 June 2007 with the IRAM¹ 30 m telescope using the A100 receiver with the VESPA correlator for H¹³CO⁺ ($J = 1-0$) at 89.188 GHz and HCO⁺ ($J = 1-0$) at 86.75 GHz. The average system temperature was ~85 K. Sources CygX-N48 and -N53 were observed on 2–5 June 2007 as part of a large-scale OTF mapping of the DR21 filament (Schneider et al. 2010), and have average system temperatures of around 110 K. The data were corrected for the main beam efficiency of 0.78 and have a velocity resolution of 0.135 km s⁻¹. The HPBW at this frequency is ~28″.

2.2.2. Observations with the Plateau de Bure Interferometer

We used the IRAM Plateau de Bure Interferometer (hereafter PdBI) to perform high angular-resolution observations at 1 mm and 3 mm. A more detailed description of the observations can be found in Paper I. We obtained line emission measurements of H¹³CO⁺ ($J = 1-0$) and H¹³CN ($J = 1-0$) at 86.75 and 86.34 GHz, respectively, with a velocity resolution of 0.134 km s⁻¹. The observations were done in track-sharing mode

with two targets per track. The D configuration tracks were obtained between June and October 2004 with five antennas with baselines ranging from 24 m to 82 m. The C configuration tracks were obtained in November and December 2004 with six antennas in 6Cp configuration and baselines ranging from 48 m to 229 m. As a phase calibrator, we mostly used the bright nearby quasar 2013+370 and as a flux calibrator the bright evolved star MWC349 located in Cygnus-X.

2.3. Data reduction and cleaning

We used the GILDAS software² for the data reduction and analysis of single-dish and interferometric data. The interferometric H¹³CO⁺ dataset was reduced both with and without adding short-spacing information, which was obtained with the IRAM 30 m telescope and implemented with the standard techniques of GILDAS. No zero-spacing information was available for the H¹³CN dataset. For the cleaning procedure, we used a naturally weighted beam to search for clean components within a circle. The resulting parameters of the data reduction are summarized in Table 1. All maps are corrected for primary beam attenuation.

3. Results

As a continuation of the interferometric mm-continuum studies of Paper I, we focus on a study of the distribution and the kinematics of dense gas traced by HCO⁺, H¹³CO⁺, and H¹³CN in our sample of MDCs. We first present single-dish maps of HCO⁺ and H¹³CO⁺, on which we later base our radiative-transfer line modeling in Sect. 4.1.2. Spectra from both single-dish and interferometric maps are then shown, followed by line-integrated maps of H¹³CO⁺ and H¹³CN.

3.1. IRAM 30 m H¹³CO⁺ and HCO⁺ observations

Spectral line maps of the IRAM 30m observations of the five MDCs are shown in Fig. 2a. We obtained a map of line emission of ~1 arcmin² for the three isolated MDCs (CygX-N3, -N12, -N63). For CygX-N48 and -N53, we cut out maps from a larger mapping of Schneider et al. (2010) with the same dimensions.

Both lines are clearly detected over the extent of MDCs on a size-scale of ~0.1 pc. The large-scale distribution of emission indicates a rich gas content in all cores. For the isolated cores (CygX-N3, -N12, -N63), the distribution of H¹³CO⁺ emission is centrally peaked and confirms the core as a coherent entity. For the fields located in the DR21 filament, the distribution of

¹ IRAM is supported by INSU/CNRS (France), MPG (Germany) and IGN (Spain).

² See <http://www.iram.fr/IRAMFR/GILDAS/>

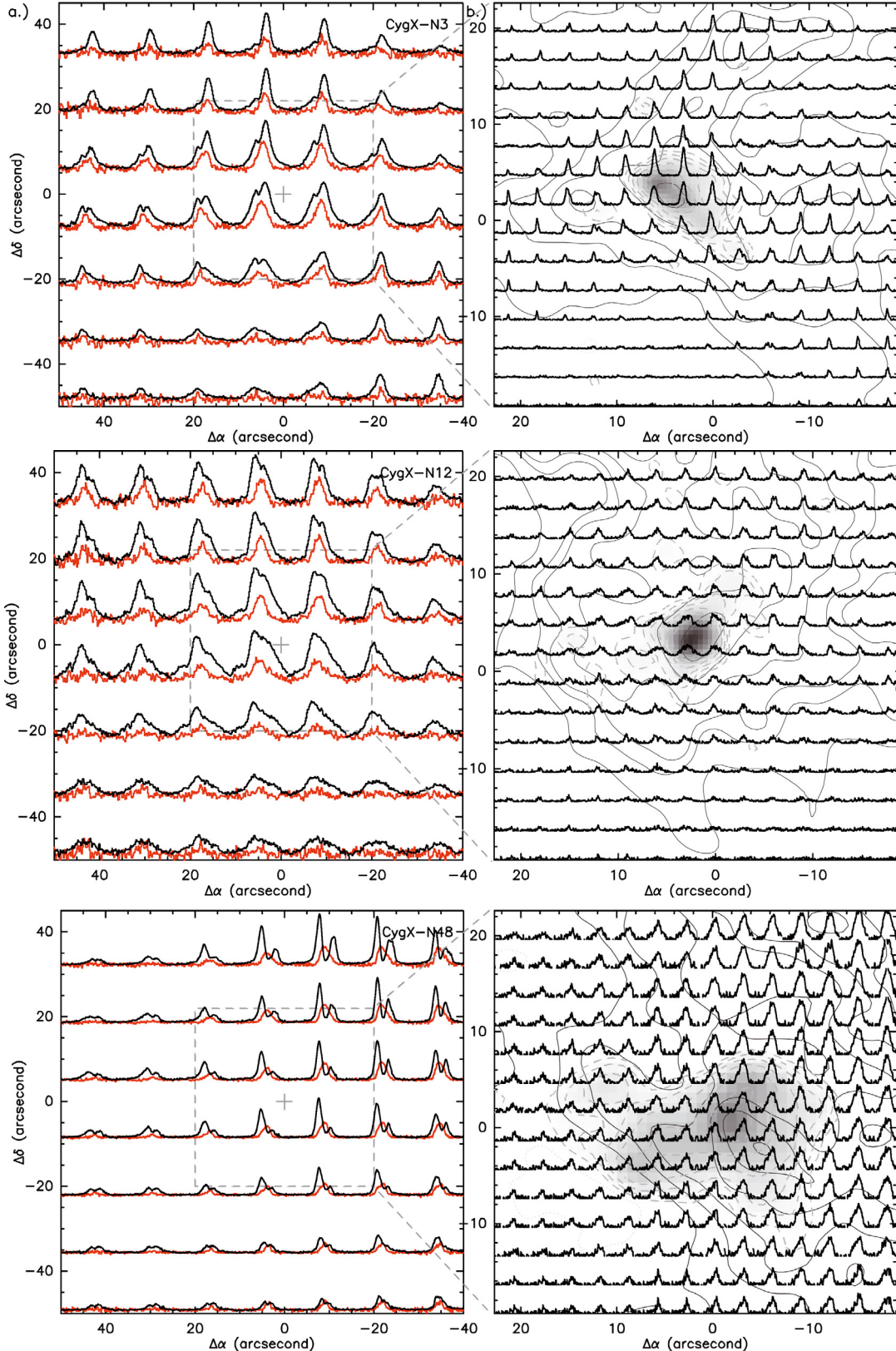


Fig. 2. a) Spectral line maps of HCO⁺ (black) and H¹³CO⁺ (red) obtained with the IRAM 30m telescope and regridded to full-sampling. The velocity range is 10 to 20 km s⁻¹ for CygX-N3, -N12, -15 to +5 km s⁻¹ for CygX-N48 and CygX-N53, -10 to 0 km s⁻¹ for CygX-N63. The intensity of the optically thin line (H¹³CO⁺) is scaled up by a factor of 2–4. Dashed squares indicate the size-scale of the right panel. b) Spectral line maps of H¹³CO⁺ PdBI combined with IRAM 30m, where the spectra-cubes were regridded to 3'' resolution. Velocity ranges are 10 to 20 km s⁻¹ for field CygX-N3, -N12 and -10 to 0 km s⁻¹ for CygX-N48, -N53 and -N63, respectively. The gray-scale background image is the 3 mm continuum emission obtained simultaneously with the PdBI (from 3 σ to 75 σ). (The gray dashed contours show the (logarithmic) contour levels of 3 σ , 4.8 σ , 7.5 σ , 12 σ , 19 σ , 30 σ , 75 σ , and 120 σ , where σ is between 0.17 to 0.33 mJy/beam similarly as in Paper I.) Gray solid line contours show the integrated intensity maps of H¹³CO⁺ (same as in Fig. 4a).

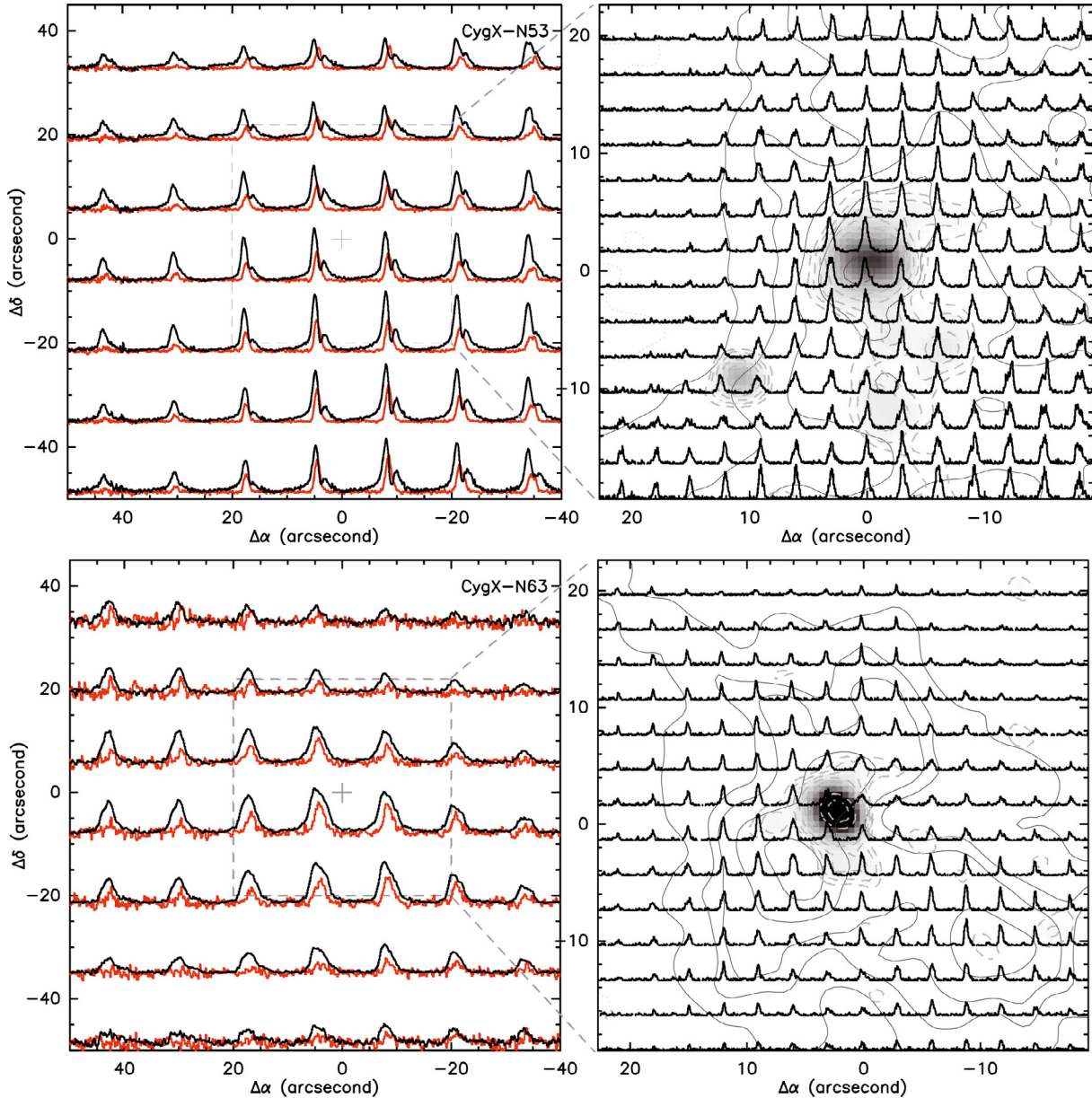


Fig. 2. continued.

emission follows the main pattern of the filament and therefore shows a strong north-south elongation.

The H^{13}CO^+ line shape is a rather clear Gaussian in CygX-N53 and -N63, while in the other fields it shows a nearly Gaussian profile. The blending of several components and broad line-wings are remarkably apparent in CygX-N3 and CygX-N12. Towards CygX-N48 a red-shoulder is present in the spectra, while the stronger component is centered on the self-absorbed profiles of HCO^+ that appear to contain two strong components in the spectra.

The optically thick tracer, HCO^+ , shows blue-shifted asymmetry in four MDCs of our sample. In CygX-N3, this profile changes into a red-shifted asymmetry over a part of the map. The dip is at the same velocity where the optically thin line peaks, which is commonly interpreted as an expanding envelope or an outflow feature (Myers et al. 1996). However, $\sim 15''$ away from the center the profiles turn into a standard infall profile. These blue-shifted asymmetric profiles are observed

towards CygX-N48 and -N53. In all these cases, the dip of self-absorption is located at the peak of the optically thin line indicating infall. Interestingly, CygX-N12 and especially CygX-N63 show only a slight asymmetry in their spectra. Since the ratio of H^{13}CO^+ and HCO^+ line intensities (7, 5.5, 5.5, 1.9, 3.7 for CygX-N3, -N12, -N48, -N53, -N63, respectively) indicate that the emission of HCO^+ must be optically thick, we interpret this blue-shifted asymmetry as an infall signature. In Sect. 4.1.2, we present radiative transfer modeling of these line profiles.

3.2. IRAM PdBI H^{13}CO^+ and H^{13}CN observations

3.2.1. IRAM PdBI H^{13}CO^+ spectra maps

Maps of H^{13}CO^+ spectra obtained with the PdBI and processed with zero-spacings are presented in Fig. 2b. We regridded the spectra-cubes to a fully sampled synthetic HPBW of $\sim 4''$. These maps of spectra taken at high angular-resolution resolve several

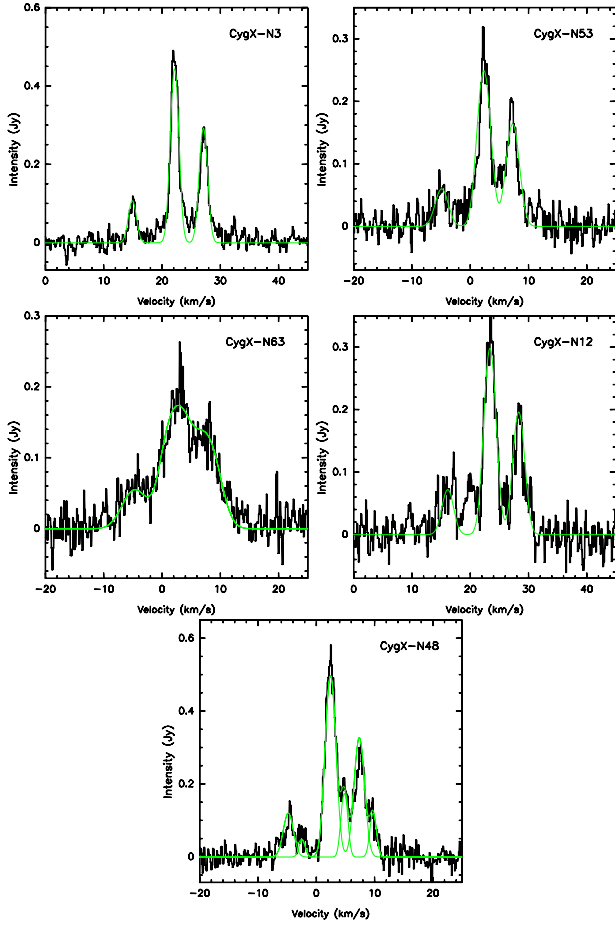


Fig. 3. HFS line fitting of the H^{13}CN spectra, which were averaged within 50% contours of the peak emission. (Note that two components could be fitted to CygX-N48.) Green line indicates the result of HFS line-fitting assuming LTE conditions. All hyperfine-components are detected towards all of the cores.

distinct spectral components. For fields CygX-N3 and -N53, individual spectral components are found with a separation of $0.5\text{--}2\text{ km s}^{-1}$ ($4\times\text{--}15\times$ the spectral resolution). They appear to be clearly offset from the main position of the continuum peaks and can be separated into two strong components each of them showing a shift in both position and velocity and a tendency to blend into a single line towards the continuum peaks. In fields CygX-N12 and -N48 the spectra are more complex, especially in CygX-N12 where the spectra are flat topped making the separation of the components difficult. Similarly in CygX-N48 the two strong components seem to be blended with other components and in the central region broad lines can be seen. We note that for CygX-N48 a large-scale sub-filament at 0 km s^{-1} is reported by Schneider et al. (2010) to the north-east, towards DR21(OH). CygX-N63 is dominated by a single component and a weak one appears separated by $\sim 0.5\text{ km s}^{-1}$.

3.2.2. IRAM PdBI H^{13}CN spectra

H^{13}CN spectra were integrated within the 50% level of the peak emission and are shown here with the corresponding hyperfine-structure (HFS) fits for each source (Fig. 3). The strongest lines are observed towards CygX-N3 and CygX-N48, while the other cores are weaker, but all 3 hyperfine components are detected. A larger line-width component around the main peak of the line is seen towards CygX-N3, -N53, but it is strongest in CygX-N63.

The H^{13}CN line-profile towards the core CygX-N63 is a single, broad component, which significantly differs from all the other fields likely because of outflows. Two individual components can be seen towards CygX-N48.

The HFS fitting, which assumes LTE conditions reproduces well the line profiles. The measured line ratio for the $\frac{F=0\rightarrow 1}{F=2\rightarrow 1}$ hyperfine component is 0.265 ± 0.065 and for the $\frac{F=1\rightarrow 1}{F=2\rightarrow 1}$ hyperfine components is 0.668 ± 0.102 . This is close to the intensity ratios expected in LTE, which is 0.2 for the $\frac{F=0\rightarrow 1}{F=2\rightarrow 1}$ and 0.6 for the $\frac{F=1\rightarrow 1}{F=2\rightarrow 1}$ hyperfine component (e.g. Guilloteau & Baudry 1981).

3.3. High angular-resolution integrated intensity maps

3.3.1. H^{13}CO^+ integrated intensity maps

The integrated intensity maps obtained for the H^{13}CO^+ lines are presented in Fig. 4a, b. For comparison, contours of 3 mm continuum emission from Paper I are shown. We note that the two maps have a similar spatial resolution of $\sim 4''$. In all cores we detect strong line-emission with the PdBI, which resolves significant substructures of molecular gas compared to the IRAM 30 m observations because of its about seven times better angular resolution.

The integrated intensity maps of H^{13}CO^+ including zero-spacings are shown in Fig. 4a. Including the zero-spacings allows us to also recover emission from larger spatial scales. The large-scale emission enhances the asymmetry in the emission from CygX-N48 and -N53, which are associated with a large-scale structure, the DR21 filament. CygX-N53 is located towards the northern tip of the filament and shows an intensity distribution in the north-south direction, which becomes stronger towards the main part of the filament located south of the maps. For field CygX-N48, the distribution of the molecular gas emission is strongly asymmetric and drops towards the south-western edge of the core, close to a compact cluster of embedded young stars. On the other hand, towards the opposite, north-east direction the emission gets significantly stronger. This shows the same morphology as the large-scale emission of H^{13}CO^+ , which is also presented in Fig. 5 of Schneider et al. (2010).

Figure 4b and c show maps of integrated intensity of H^{13}CO^+ and H^{13}CN , respectively, using only interferometric data (no zero-spacings added). The distribution of dense molecular gas within the 0.1 pc-scale is highly non-uniform and shows significant substructure. The strongest line emission is generally observed towards the central regions of the cores, and coincides well with the 3 mm continuum peaks (indicated by gray contours). Only CygX-N63 is distinctive because there is a prominent “hole” in the H^{13}CO^+ emission towards the continuum emission. The two lobes surrounding the continuum peak suggest that H^{13}CO^+ is highly depleted (see Sect. 4.1.2) and emission is completely absent towards the central densest regions.

3.3.2. H^{13}CN integrated intensity maps

The emission of H^{13}CN (Fig. 4c) always peaks at the brightest continuum sources and thus the densest parts of the MDCs. Comparing the distributions of the emission of H^{13}CO^+ and H^{13}CN , they both trace the densest parts of the MDCs, but are locally different. In CygX-N3, all the important continuum peaks are embedded in emission of dense molecular gas, except for CygX-N3 MM4 (following the notations of Paper I), which is outside the brightest H^{13}CN emission peak. In addition, the north-western lobe that appears strongly in H^{13}CO^+ ,

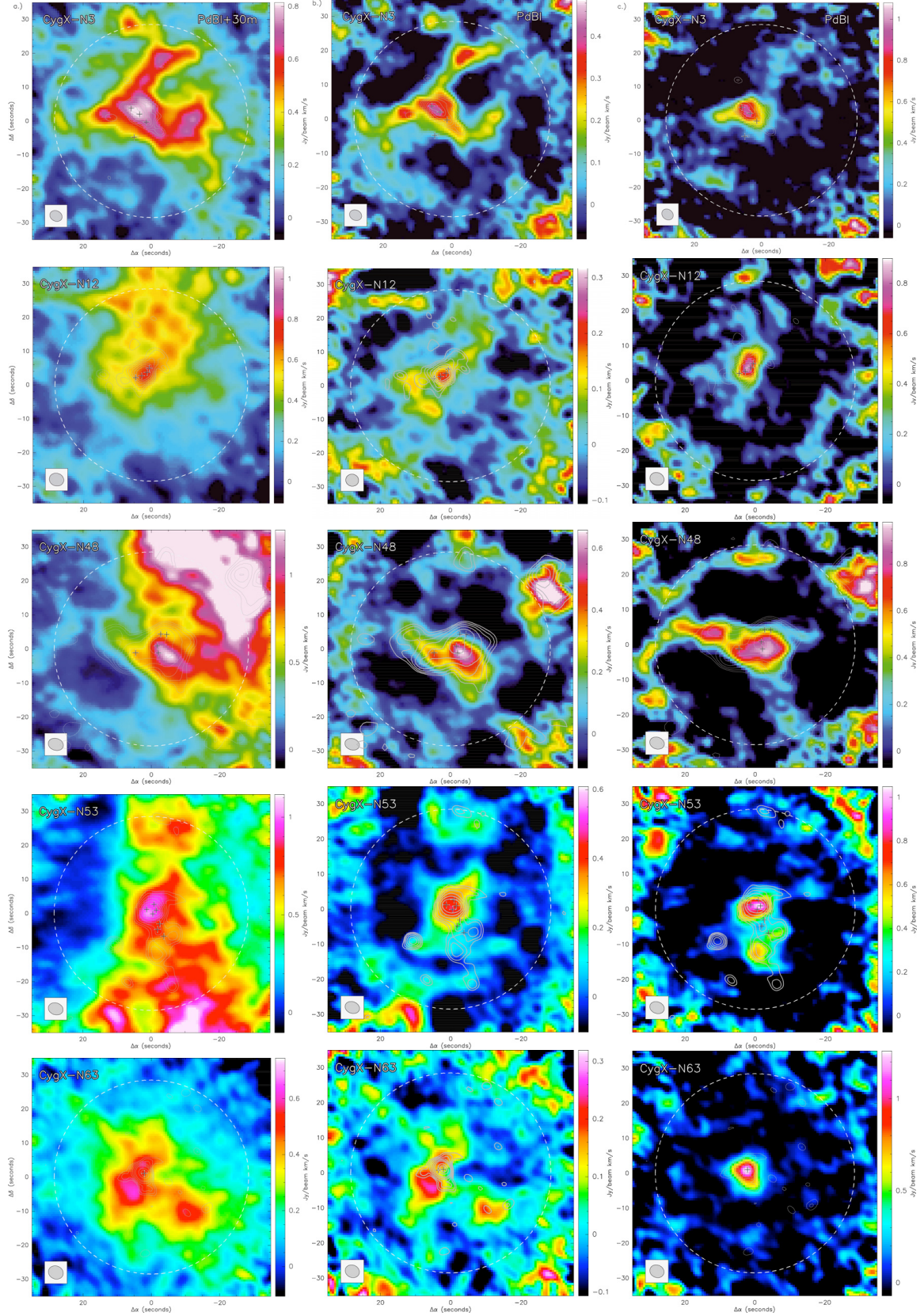


Fig. 4. **a)** Integrated intensity maps of H^{13}CO^+ ($J = 1-0$) obtained with PdBI and combined with observations from the IRAM 30 m telescope (the scaling goes from -2σ to 35σ for field N63 and N12, and from -2σ to 60σ for all other fields). Contours show the 3 mm continuum emission, where levels are the same as in [Paper I](#). Crosses indicate the location of 1 mm continuum sources reported in [Paper I](#). Dashed circles indicate the primary beam of the PdBI. Gray ellipses in the *left lower* corner show the synthesized beam. **b)** Interferometric line-integrated intensity maps of H^{13}CO^+ ($J = 1-0$). **c)** Integrated line intensity maps of H^{13}CN ($J = 1-0$) (over all hyperfine components).

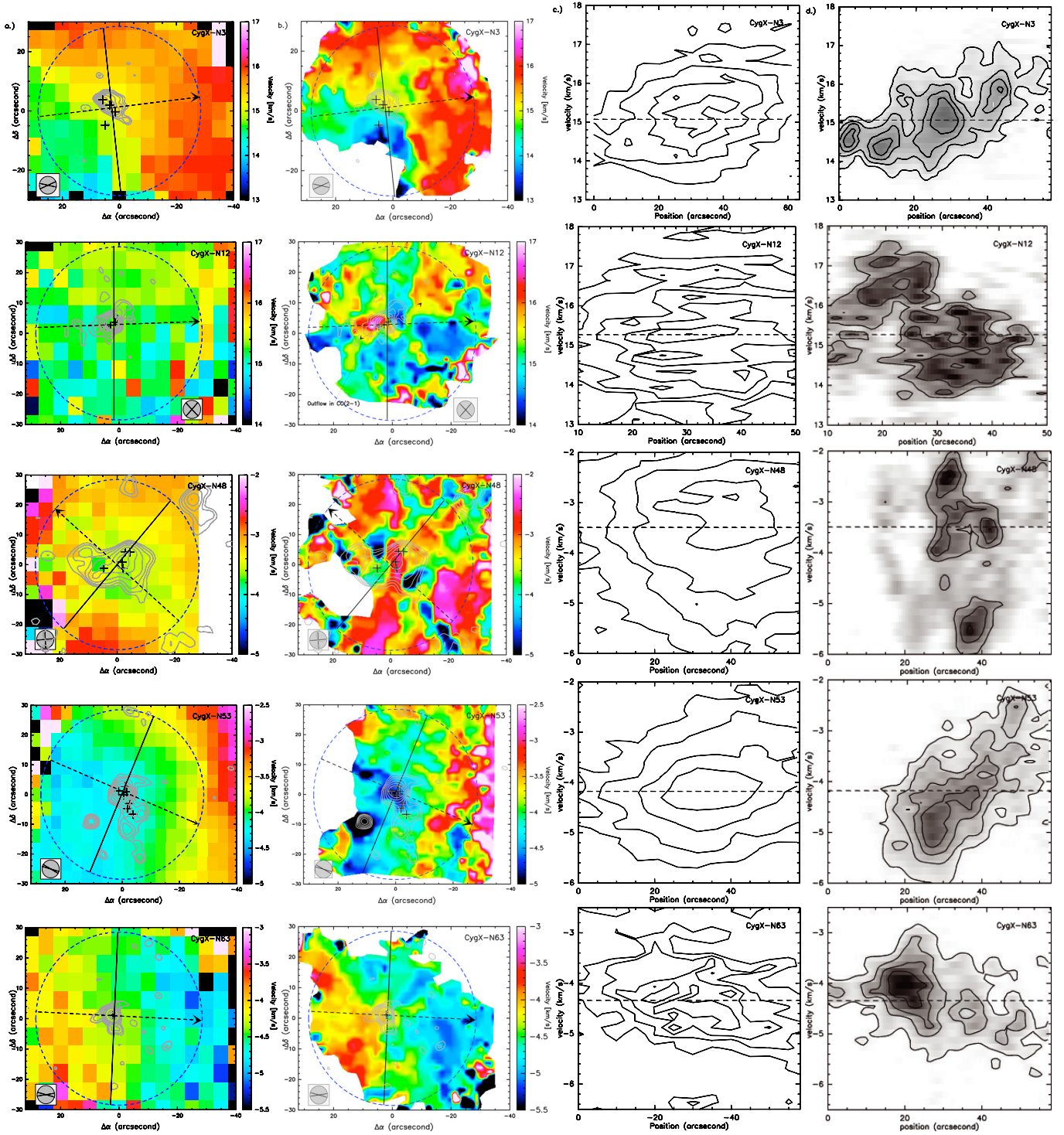


Fig. 5. **a)** The maps show the velocity-field of the single-dish maps of H^{13}CO^+ , which is obtained by a single Gaussian fit. Dashed circles show the primary beam size of the PdBI. Dashed lines show the axis of the velocity gradient, while the arrows indicate the position angle of the gradient. The error of the gradient fitting is shown in the lower corners of the images. **b)** The maps show the peak velocity of the PdBI+30 m H^{13}CO^+ spectra. **c)** Position-velocity cuts of the single-dish H^{13}CO^+ spectra-cubes along the velocity gradient derived in Sect. 4.2.1 and indicated on **a)**. Contour levels go from 20% of the peak intensity by 20% levels. Dashed lines indicate the systemic velocity. **d)** IRAM 30 m+PdBI position-velocity cuts along the same direction. Contour levels indicate 20% of the peak emission as well and increase by 20% for CygX-N3, -N53, -N63, while contours start at 50% of the peak for CygX-N12, -N48.

is weak in H^{13}CN , which may be indicative of chemical differences within the cores. CygX-N12 has a central peak embedded in an elongated, filamentary-like emission in continuum, which is similarly traced by weak H^{13}CO^+ emission. Nevertheless, in H^{13}CN only the main peak of continuum is traced. The 3 mm

continuum and molecular line emission in CygX-N48 is more diffuse and follows an east-west elongation. In CygX-N53, the central continuum peak is traced well in both molecules, but while the southern lobe contains two peaks in continuum and is well-traced by H^{13}CN , it is absent in H^{13}CO^+ . A compact

Table 2. Result of line-fitting to single-dish H^{13}CO^+ lines (28'' angular resolution).

Source	$\int T_{\text{mb}} dv$ [K]	v_{lsr} [km s ⁻¹]	$\sigma_{\text{H}^{13}\text{CO}^+}$ [km s ⁻¹]	$\sigma_{\text{N}_2\text{H}^+}$ [km s ⁻¹]
CygX-N3	4.77 ± 0.1	15.07 ± 0.03	1.01 ± 0.02	0.98
CygX-N12	3.30 ± 0.11	15.27 ± 0.05	1.23 ± 0.05	0.89
CygX-N48	5.02 ± 0.14	-3.49 ± 0.04	1.26 ± 0.04	1.28
CygX-N53	5.54 ± 0.13	-4.18 ± 0.02	0.9 ± 0.03	0.76
CygX-N63	2.54 ± 0.09	-4.34 ± 0.03	0.69 ± 0.03	0.72

Notes. We show the main-beam brightness temperature, local rest velocity and velocity dispersion of the line. The velocity dispersions obtained with single-dish N_2H^+ pointed observations towards these cores is shown for comparison in the last column (Paper I).

3 mm continuum peak (probably a more evolved protostar) is found south-west of the central peak, which appears in H^{13}CO^+ , but is not seen in H^{13}CN . As mentioned before, the main peak of CygX-N63 is absent in H^{13}CO^+ , but is clearly detected as strong, compact emission of H^{13}CN .

Summarizing, H^{13}CN is generally more centrally peaked than H^{13}CO^+ . These differences in the distribution of the two lines may be explained by physically different environments, thus different excitation conditions and/or abundance anomalies close to massive protostars.

4. Analysis

4.1. Analysis and modeling of the single-dish spectra of HCO^+ and H^{13}CO^+

4.1.1. Line-fitting of single-dish H^{13}CO^+ spectra

The single-dish maps of H^{13}CO^+ ($J = 1-0$) show a single line detected over a significant extent in each core, thus we fit them to first order with a Gaussian. We use the result of the fit to derive the parameters of the spectra: line intensity, the local rest velocity (v_{lsr}), and the line-width (and dispersion $\sigma = \frac{\text{FWHM}}{\sqrt{8 \ln(2)}}$) in each core and assume that H^{13}CO^+ is optically thin. The values for each core at the position of the PdBI phase center are listed in Table 2.

The emission associated with cores CygX-N3 and -N12 have a v_{lsr} of +15 km s⁻¹, while cores CygX-N48 and -N53 have a v_{lsr} of -3.5 and -4.2 km s⁻¹, respectively. These two cores are located in the massive filament associated with DR21 and their rest velocity is consistent with that of the filament, confirming that they are physically associated. CygX-N63 is located southwards of the filament, but is associated with the south tail of the large-scale complex of DR21 and DR23 in Cygnus-X North with a v_{lsr} of -4.3 km s⁻¹ (Schneider et al. 2006).

We derive velocity dispersions of the orders of ~ 1 km s⁻¹ for the cores, which is similar to N_2H^+ observations from Paper I, though three of the latter are smaller (by $\sim 0.1-0.2$ km s⁻¹) (Table 2). We note that the largest line-dispersions are observed towards the most massive core, CygX-N48 (see also in Sect. 5.2).

4.1.2. Radiative transfer modeling

Radiative transfer modeling of the single dish spectra of H^{13}CO^+ and HCO^+ was performed simultaneously using

the 1D spherical, non-LTE radiative transfer code *Simline* (Ossenkopf et al. 2001). The spectra of H^{13}CO^+ and HCO^+ were extracted for each MDC at the center position of the single-dish maps and then averaged in concentric annuli in steps of 14'' with respect to this position. The physical model used for all MDCs is described in detail in Appendix A. (See also Figs. A.3 to A.7).

We used continuum data to derive the mass, thus the density profile, and NH_3 data (Wiener 2008) to constrain the temperature profile, and varied only the density at which depletion sets in and the depletion ratio for each core within a range of 10^5 to 10^6 cm⁻³ and 0–1000, respectively. The best-fit results correspond to optically thick emission of HCO^+ ($\tau \sim 8.3$ to 15.4) and optically thin H^{13}CO^+ ($\tau \sim 0.3$ to 0.5) emission in all MDCs. We find that introducing depletion at a density of $\sim 10^6$ cm⁻³ with a depletion factor of 50–100 generally provides good line intensities. Only within the coldest and densest MDC, which is CygX-N63, depletion had to be introduced at a lower density of $\sim 2 \times 10^5$ cm⁻³. With this modeling, we show that for the optically thin cases the emission is dominated by the outer layers and not the regions close to the center, where depletion is high. This indicates that the emission originates more from the bulk of material with densities of 10^4-10^6 cm⁻³, corresponding to the inter-protostar medium, i.e., the mass reservoir of the core.

4.2. Velocity field

4.2.1. Global velocity field: rotation-like patterns?

The systematic shifts seen in the line-positions were studied to understand the global kinematics of MDCs. We derive the velocity field with the Gaussian line-fitting procedure to the H^{13}CO^+ maps of the IRAM 30 m telescope (see Fig. 5). CygX-N3, -N53, and -N63 show a homogenous, but clearly non-isotropic velocity field with a systematic, axi-symmetric shift in the line position (velocity). In CygX-N53, this velocity pattern follows the global velocity field of the DR21 filament (Schneider et al. 2010). Towards CygX-N12 and CygX-N48, no clear global pattern is seen, the velocity field appearing to be rather random. Figure 2b indicates that in CygX-N12 a single Gaussian fit may not reproduce well the observed line profiles because of the blending of more components. Similarly, for CygX-N48 a second component is seen as a weak shoulder on the spectra, therefore a single Gaussian fit for these two MDCs may not be representative of the velocity field.

Altogether, for three out of five MDCs a rotation-like velocity pattern is visible. To derive the axis and position angle of the velocity shift, we use the least squares fit approach of Goodman et al. (1993). We applied the routine *VFIT*³ (Goodman et al. 1993) to derive velocity gradients from the velocity field. The results are shown in Table 4 and the position angle of the resulting gradients are indicated in Fig. 5. The derived angle corresponds well to the observed axi-symmetry of the velocity field. The velocity gradients have the same order of magnitude of what has been observed for low-mass nearby cores (Goodman et al. 1993; Caselli et al. 2002), between 1.2–4.2 km s⁻¹ pc⁻¹. The highest gradient is seen in CygX-N53, while in CygX-N12 and -N48 no gradients can be derived. Among the three cores, where the velocity field follows a clear symmetry, the smallest gradient is associated with the least massive but most compact core (containing only one massive protostar), while the largest is in CygX-N53, which is embedded in the DR21 filament. This filament has very complex kinematics with large gradients. The velocity

³ IDL routine for performing a least squares fit to the velocity field.

gradient of CygX-N53 is consistent with previous estimates of Schneider et al. (2010) indicating that this core is embedded and kinematically linked to the filament.

4.2.2. Small-scale velocity field

We compare the velocity field obtained with single-dish, low angular-resolution data with the high angular-resolution observations obtained with PdBI (and zero-spacings). Since the spectra show several lines dispersed within a few km s^{-1} , a single Gaussian fit cannot be representative of the velocity field. Therefore we extract and map the peak velocity of the spectra, which results in a velocity field tracing the bulk of motions (see Fig. 5 right panel).

At high angular-resolution, the axisymmetric global velocity pattern is resolved into more substructures in velocity, indicating a much richer dynamics. Despite the small-scale velocity fluctuations, in three MDCs the velocities are dominated by a large-scale gradient. CygX-N3, -N53, and -N63 show a remarkably symmetrical global velocity field with systematic shifts in velocity, consistent with the single-dish maps. The velocity field in CygX-N12 and -N48 lack clear gradients and are dominated by fluctuations on small-scales, which make it very complex. Within CygX-N12, a strong outflow is observed in ^{12}CO ($J = 2-1$) (Bontemps et al., in prep.), which may also be apparent in the velocity field map as indicated in Fig. 5. Towards CygX-N48, the velocity field is complex without any clear trends of systematic motions. The complexity of the velocity fields of CygX-N12 and CygX-N48 is due to the presence of several spectral components, which are also seen in Fig. 2.

4.3. Position-velocity diagrams

Position-velocity cuts were taken along a cut through the continuum peaks and perpendicular to the axis derived from the fit to the velocity fields. In Fig. 5c, contours of the position-velocity maps of the single-dish observations are shown. The velocity gradients towards CygX-N3, -N53 and -N63 are clearly seen. For CygX-N12 and -N48, a large dispersion in velocity becomes obvious, which explains the complexity of the velocity field maps.

Figure 5d shows the position-velocity maps along the same cuts from the high-resolution IRAM 30 m+PdBI data. In all cases, we resolve much richer structures confirming the existence of several line components and gradients. For CygX-N3, -N53, and -N63, these velocity cuts perhaps illustrate most clearly the complexity of velocity features obtained with the high angular-resolution data. In CygX-N3, the pv-map shows a clumpy structure with several peaks showing a gradient across the range $\sim 14.5-16 \text{ km s}^{-1}$. The peaks correspond to individual structures at different positions, but we point out that they must be physically linked, being embedded in the same flow of gas and consistent with the velocity gradient seen in the single-dish data. In CygX-N53 and -N63, the velocity shift is smooth (less clumpy) and goes from ~ -5.5 to -3.5 km s^{-1} and from -3.5 to -5 km s^{-1} , respectively.

For CygX-N12 and -N48, we resolve for the first time indications of velocity gradients. In these two plots (Fig. 5d, middle panels), we increased the contour levels to show only the 50% level of the peak emission, since there is emission coming from broad line-wings because of outflows. For CygX-N12, the gradient goes from 17 km s^{-1} down to 14 km s^{-1} , while CygX-N48

Table 3. Result of HFS line-fitting of the PdBI H^{13}CN line.

Source	$\int I dv$ [Jy/beam]	v_{lsr} [km s^{-1}]	$\sigma_{\text{H}^{13}\text{CN}}$ [km s^{-1}]	τ
CygX-N3	0.113 ± 0.002	14.96 ± 0.12	0.69 ± 0.03	0.1
CygX-N12	0.076 ± 0.002	16.16 ± 0.29	0.98 ± 0.07	0.1
CygX-N48-1	0.05 ± 0.01	-2.39 ± 0.04	0.53 ± 0.1	0.15
CygX-N48-2	0.127 ± 0.002	-4.77 ± 0.02	0.86 ± 0.05	0.1
CygX-N53	0.063 ± 0.001	-4.87 ± 0.03	1.1 ± 0.06	0.1
CygX-N63	0.063 ± 0.006	-4.64 ± 0.1	2.05 ± 0.22	0.271

Notes. The H^{13}CN is taken from an average within the contour of 50% of the peak emission: peak intensity, local rest velocity, velocity dispersion and opacity. The same excitation temperature is assumed for all components.

Table 4. Result of least squares fitting to the velocity gradient of the IRAM 30 m H^{13}CO^+ maps: velocity gradients and positions angles.

Source	\mathcal{G} [$\text{km s}^{-1} \text{ pc}^{-1}$]	PA [$^\circ$]	β	J/M [$\text{km s}^{-1} \text{ pc}$]
CygX-N3	1.97 ± 0.7	96	30×10^{-4}	7.88×10^{-3}
CygX-N12	0.42 ± 0.43	-89	1.5×10^{-4}	1.68×10^{-3}
CygX-N48	0.68 ± 0.7	46	4.2×10^{-4}	5.33×10^{-3}
CygX-N53	4.17 ± 0.7	67	250×10^{-4}	20.9×10^{-3}
CygX-N63	1.17 ± 0.34	-93	4×10^{-4}	1.86×10^{-3}

Notes. From the systematically derived velocity gradients, we calculated the β parameter ($E_{\text{rot}}/E_{\text{pot}}$) and the specific angular momentum, respectively. Note that towards CygX-N12 and -N48, no gradient was found.

has two components: one dispersed between -2 and -4 km s^{-1} , the other component at $\sim -5.5 \text{ km s}^{-1}$.

These velocity gradients, as seen for CygX-N3, -N53, and -N63, can be interpreted in the framework of rotating structures. In the case of solid body rotation, velocity scales linearly with the position, which could be consistent with the pv-maps for CygX-N3, CygX-N53, and CygX-N63. For the other fields, solid body rotation is unlikely due to the complexity of the individual velocity components. The origin of the velocity pattern is discussed in Sect. 5.2.2.

4.4. H^{13}CN spectra

We performed HFS line-fitting to the extracted H^{13}CN spectra for each core and summarize the results in Table 3. For CygX-N3, -N12, -N53, and -N63 we obtain a good fit with only a single line, but we indeed identify two components for CygX-N48 at -4.77 km s^{-1} and -2.39 km s^{-1} . The line velocities of H^{13}CN are in good agreement with the velocity of the H^{13}CO^+ line ($\pm 0.2 \text{ km s}^{-1}$) towards CygX-N3, and -N63, while for CygX-N12 and -N53 they differ by $\sim 0.8 \text{ km s}^{-1}$ from the H^{13}CO^+ line. The reason behind this is not clear, but may indicate that there are chemical differences on the projected size-scales of $\sim 10\,000 \text{ AU}$ and these two tracers may not trace the same gas. The HFS fitting in Fig. 3 suggests that the assumption of LTE excitation condition is satisfactory for all MDCs.

In Sect. 3.2.2, we noted already the ‘‘bump’’ in the spectra, peaking at the position of the main line with a large plateau on the two sides. We further investigated the possible origin of this feature by searching for complex molecules at these frequencies but found no lines that could result in such a strong contribution.

This is the most prominent feature in CygX-N63, where the line-dispersion is surprisingly large ($\sim 2 \text{ km s}^{-1}$) compared to the other MDCs. We discuss in detail the possible origin of that in Sect. 5.1.2.

5. Discussion

From a theoretical point of view, there is either a high level of turbulence in the MDCs, capable of providing significant support against gravity to allow a quasi-static evolution towards the monolithic collapse of the cores, or the cores are not in equilibrium and their formation and evolution is mostly driven by dynamical processes. Specific and different kinematics is expected in the two scenarios (e.g. supersonic micro-turbulence versus complex, but organized flows).

We first discuss the origin of the observed line emission (Sect. 5.1), then we analyze the physical origin of the velocity dispersion on large ($\sim 0.1 \text{ pc}$) and small scales ($\sim 0.03 \text{ pc}$, Sect. 5.2) to assess the amount of micro-turbulence in the cores that could stabilize and regulate their evolution. We finally review the obtained results in the context of the two competing scenarios (Sect. 5.3).

5.1. Molecular lines tracing high-density material

5.1.1. H^{13}CO^+ traces the inter-protostar medium

H^{13}CO^+ has often been detected around low-mass protostars following an elongated structure perpendicular to their outflow. Having a high critical density, it is acknowledged as a good tracer of low-mass protostellar envelopes (e.g. Saito et al. 2001; Jørgensen et al. 2004). The average density in our sample of MDCs is high ($> 10^5 \text{ cm}^{-3}$) (Motte et al. 2007), while the peak density in protostars estimated in Paper I reaches up to $\sim 10^7 - 10^8 \text{ cm}^{-3}$. These MDCs lack significant emission at infrared wavelengths, and NH_3 measurements (Wienen 2008) confirm that they are cold with kinetic temperatures of 18–28 K, CygX-N63 being the coldest and CygX-N48 the warmest one. Such high densities at low temperatures should lead to a high level of depletion of virtually all C-bearing molecules as a consequence of CO depletion onto grains (e.g. Tafalla et al. 2002; Bergin & Tafalla 2007). On the other hand, the desorption temperature for CO is of the order of 20 K, i.e. similar to the observed temperatures here, considering also that if protostars have formed already, they might heat-up their cold environment, releasing and restarting the formation of C-containing molecules. The precise level of depletion is therefore uncertain and the abundances of different molecules (here H^{13}CO^+ and H^{13}CN) as a function of density and temperature is even more difficult to predict.

From our radiative transfer modeling (Sect. 4.1.2, Appendix A, and Figs. A.3–A.7), we conclude that H^{13}CO^+ is always optically thin and the emission is dominated by the gas between the protostars and cannot probe their highest densities because of significant depletion in their central regions. We find indications of the highest depletion towards CygX-N63, where in its central regions a significantly higher depletion ratio and lower depletion density was used to reproduce the correct line intensities. Summarizing this picture, we base the following discussion on assuming that the emission of H^{13}CO^+ comes from the dense material within the MDC, but represents the bulk of material in which the protostars are embedded, instead of their inner envelope as for low-mass protostars.

5.1.2. H^{13}CN , a better tracer of the highest density regions?

Modeling of e.g. Lee et al. (2004) has shown that HCN may also be affected by depletion, but to a somewhat lower level than HCO^+ . In surveys of low-mass pre-stellar cores, Sohn et al. (2007) observed that HCN traces more closely the inner part of the cores than HCO^+ and shows a similar distribution as N_2H^+ , which is known to trace the inner (dense, cold) part of the cores (Tafalla et al. 2006; Di Francesco et al. 2007).

Nevertheless, Lee et al. (2004) also pointed out that HCN is part of a complex chemical network, whereas HCO^+ may depend on the CO abundance. Based on the morphology of the emission distribution presented in Fig. 4, we show here that H^{13}CN has a better correspondence with the central higher density regions (continuum peaks) than H^{13}CO^+ . The most prominent example is CygX-N63, where H^{13}CO^+ is completely depleted while H^{13}CN peaks at the strong continuum source. The reason for this may be twofold: H^{13}CN may simply be less depleted – as already pointed out in examples of low-mass cores, and/or H^{13}CN may be affected by different chemistry, with for instance overabundance due to strong shocks emerging from the close vicinity of the protostars.

5.2. Micro-turbulence and bulk motions within the MDCs

The analysis of line-widths constrains the relative contribution of thermal and non-thermal motions. The non-thermal velocity dispersion is usually interpreted as isotropic turbulence down to small scales where it is often referred to as micro-turbulence. However, it may have contributions from bulk motions, such as rotation, infall, and coherent flows or streamings. It is of high importance to measure the true level of micro-turbulence since this leads to a local support of a similar nature as thermal motions and thus contributes to the global support of the cores against gravity.

We first compare the global velocity dispersion to previous measurements (Sect. 5.2.1). The analysis of the single dish observations showed that the line widths of H^{13}CO^+ for most of the observed MDCs have contributions from systematic, global motions that are not micro-turbulence, but instead rotation (Sect. 5.2.2) and infall (Sect. 5.2.3). The high-resolution PdBI data confirm the presence of these motions but, in addition, distinguish several velocity components on small scales (see Sect. 5.2.4 below). Finally, it is only after these different contributions to the line-widths are recognized that we can discuss the possible remaining level of micro-turbulence to support the cores (Sect. 5.3).

5.2.1. Global velocity dispersion and virial equilibrium

A one-dimensional thermal velocity dispersion for H^{13}CO^+ and H^{13}CN is given by $\sigma_T = \sqrt{\frac{k_B T}{\mu_n m_H}}$, where k_B is the Boltzmann constant, T is the temperature, μ_n is the molecular weight equal to 30 and 28 for H^{13}CO^+ and H^{13}CN , respectively, and m_H is the mass of a hydrogen atom. Following Motte et al. (2007) and Paper I, we assume a temperature of 20 K, which gives a thermal velocity dispersion of 0.074 and 0.077 km s^{-1} for H^{13}CO^+ and H^{13}CN , respectively, while the observed dispersion is $\sim 1 \text{ km s}^{-1}$ (Table 2). This is much ($\sim 15\times$) larger than the thermal velocity dispersion, indicating that non-thermal motions contribute significantly to the line broadening.

Figure 6 compares the line-widths of the single dish H^{13}CO^+ (this work) and N_2H^+ lines (from Paper I) for the five MDCs

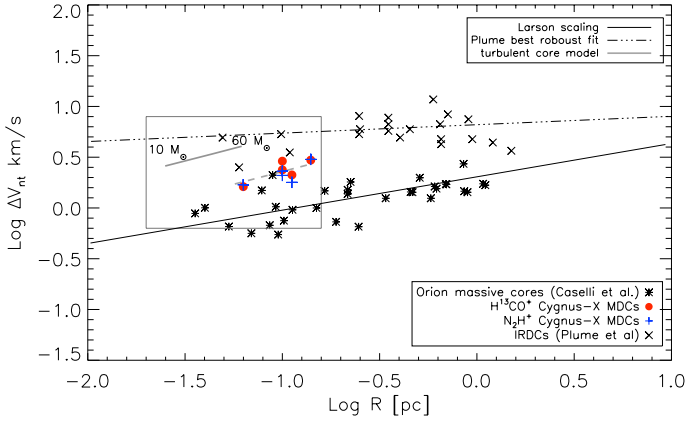


Fig. 6. We plot line-widths (FWHM) of the Cygnus-X MDCs (red large dots and blue crosses) versus the core size taken from Motte et al. (2007). Black symbols indicate line-widths taken from the literature (Caselli & Myers 1995). Black line indicates a Larson like line-widths size-relation, while the dashed-dotted line is adopted from Plume et al. (1997) representing their best robust fit to their observed line-width size-relation of IRDCs. Gray line indicates the fiducial model of McKee & Tan (2003) with a surface density of $\sim 1.7 \text{ g cm}^{-2}$ and a final stellar mass of 10 to $60 M_{\odot}$. Dashed gray line indicates the same model with a clump surface density 3 times lower. A small box indicates the data presented in Fig. 10.

with those for samples of single-dish observations of massive cores in Orion (Caselli & Myers 1995) and InfraRed Dark Clouds (IRDCs) (Plume et al. 1997). In terms of their physical properties, the Cygnus X MDCs appear to be in-between the Orion cores of Caselli & Myers (1995) and the larger distance IRDCs of Plume et al. (1997).

We use Eqs. (18) and (20) with the fiducial model assumptions of McKee & Tan (2003) to predict the turbulent velocity dispersions at a corresponding core radius required to keep the MDCs in equilibrium

$$\sigma_s [\text{km s}^{-1}] = 1.27 \left(\frac{m_{*f}}{30 M_{\odot}} \right)^{1/4} \Sigma_{\text{cl}}^{1/4} \quad (1)$$

$$R_{\text{core}} [\text{pc}] = 0.057 \left(\frac{m_{*f}}{30 M_{\odot}} \right)^{1/2} \Sigma_{\text{cl}}^{-1/2} \quad (2)$$

where the parameter m_{*f} corresponds to the final mass of the star and Σ_{cl} denotes the average clump surface density. We calculate the turbulent dispersion and the core size adopting $\Sigma_{\text{cl}} = 1.7 \text{ g cm}^{-2}$ from Paper I (which is derived using dust continuum emission) for a 10 to $60 M_{\odot}$ final star.

Our measurements on the scale of the MDCs (0.1 pc scale), which themselves represent upper limits to the turbulent support (because of other contributions to the line-width), are smaller than the model predictions of McKee & Tan (2003). The maximum level of micro-turbulence, which is observed, would only support cores with surface densities a factor of five lower than the Σ_{cl} used (see dashed line in Fig. 6).

5.2.2. Angular momentum and rotation of the MDCs

The velocity field derived from H^{13}CO^+ maps on the size-scale of the cores ($\sim 0.1 \text{ pc}$) indicates that non-thermal, organized motions such as rotation also contribute to the observed line-widths. According to Burkert & Bodenheimer (2000), if the cores were dominated by purely isotropic micro-turbulence, the velocity field should be completely random. From Fig. 5, it is clear that

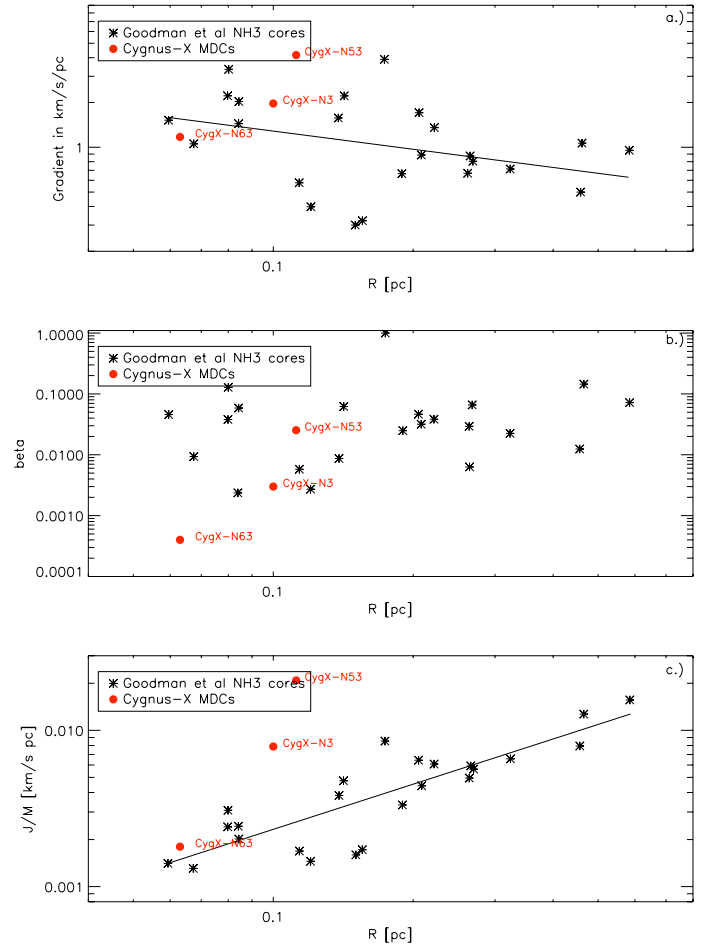


Fig. 7. a) Plot of size versus velocity gradient comparing a sample of low-mass cores (Goodman et al. 1993) with the Cygnus-X MDC sample using single-dish data. Red symbols represent the Cygnus-X MDCs, while black stars show the sample of Goodman et al. (1993). Black line shows the best-fit relation of Goodman et al. (1993) with $\mathcal{G} = 10^{-0.3 \pm 0.2} R^{-0.4 \pm 0.2}$. b) Plot of β versus size relation shown for the same sample. c) Plot of the specific angular momentum versus size. Black line shows the best-fit line from Goodman et al. (1993) with $J/M = 10^{-0.7 \pm 0.2} R^{1.6 \pm 0.2}$.

CygX-N3, -N53, and -N63 appear to exhibit indications of organized motions, while for CygX-N12 and N48 this is less obvious. For the afore mentioned MDCs, the velocity maps are axisymmetric and the axis of the symmetry is close to being aligned with the mini-filament containing the protostellar fragments. As a first order assumption, we interpret this phenomenon as rotation, which is indeed a natural consequence of preserving the initial angular momentum of the collapsing cloud. We note that the numerical simulations of Dib et al. (2010a) do report a variety of dynamical patterns for cores formed in a turbulent, magnetized, and self-gravitating molecular clouds ranging from easily recognizable rotational features such as the ones observed in CygX-N3, -N53, and -N63 to more complex features, such as the ones seen in CygX-N12 and -N48.

To discuss the observed angular momentum, we rely on the systematically derived velocity gradients. Our values of $1.2\text{--}4.2 \text{ km s}^{-1} \text{ pc}^{-1}$ are consistent with those reported in the literature for both low and high-mass objects. We also calculated the β parameter (see Table 4), which shows the ratio of the rotational to potential energy ($E_{\text{rot}}/E_{\text{pot}}$). Values between 2×10^{-3} and 1.4 were reported in a sample of low-mass cores by Goodman et al.

(1993). Our β values are low (4×10^{-4} – 2.5×10^{-2}) (see Fig. 7b) indicating that gravity dominates significantly over the rotational energy, especially in CygX-N3 and -N63. The most extreme example is the most compact core, CygX-N63 ($\beta \sim 4 \times 10^{-4}$), which hosts a single or a close-binary massive protostar. A priori, one could expect this core to behave similarly to low-mass cores, where rotating envelopes around Class 0 objects are reported. Its small velocity gradient corresponds to a very small specific angular momentum (Fig. 7c) fitting on the trend found for low mass cores by Goodman et al. (1993). Nevertheless, the other MDCs have larger specific angular momentum. We suggest that the origin of this diversity is related to the small-scale dynamics, and that the origin of the velocity field may be different for CygX-N63 and the other cores (see in Sect. 5.2.4).

In contrast, towards CygX-N12 and -N48 no clear rotation-like gradients are evident in the large-scale (~ 0.1 pc) velocity field maps with complex velocity patterns (see left panels of Fig. 5). This suggests that these two MDCs do not have a large resulting rotation in projection on the sky. Their main rotation axis may be close to the line of sight or these MDCs may have a truly smaller angular momentum than the others. In the high angular-resolution maps, some velocity gradients are indeed observed on small scales with similar velocity drifts to other MDCs, indicating that the angular momentum may be re-distributed on smaller scales.

The position-velocity cuts along the derived velocity gradient (Fig. 5 right panel) show a centrally peaked elongated pattern for CygX-N3, -N53, and -N63, which may correspond to large rotational toroids up to $40''$ (68 000 AU), $45''$ (76 500 AU), and $35''$ (60 000 AU) respectively, which may serve as a common and coherent reservoir of material for forming protostars. These rotating structures with similar size-scales were observed towards low-mass Class 0/Class I objects (e.g. Goodman et al. 1993; Caselli et al. 2002) and towards massive star-forming cores as well (e.g. Beltrán et al. 2004; Cesaroni 2005; Fallscheer et al. 2009), but the nature and origin of these rotating toroids has not yet been well established, especially in cores hosting the earliest stages of massive star formation.

5.2.3. Importance of global infall

The Cygnus-X MDCs have higher masses for the same sizes and slightly larger velocity dispersions compared to the Orion cores. The virial masses are determined in Paper I and comparing the virial-mass to mass ratios (1.16, 0.87, 1.06, 0.75, 0.51 for CygX-N3, -N12, -N48, -N53, -N63 respectively) suggests that most of the Cygnus-X MDCs may be gravitationally unstable and are therefore expected to be in global collapse. Four out of the five MDCs indeed display typical blue-shifted asymmetric HCO⁺ line profiles indicative of infall motions. As shown in Sect. 4.1.2, the line profiles of both HCO⁺ and H¹³CO⁺ can be reproduced with radiative transfer modeling with typical infall velocities in the range of 0.1–0.6 km s⁻¹. In addition to the rotation-like organized motions discussed above, this indicates that the global velocity dispersions in the MDCs also have a contribution from infall motions. The strongest infall is seen towards the most massive core CygX-N48 (~ 0.6 km s⁻¹) and is similarly large towards CygX-N53, i.e. the two MDCs located in the DR21 filament studied by Schneider et al. (2010). CygX-N3 exhibits a red-shifted asymmetric profile, which is indicative of expansion. However, the strong peak observed at ~ 16.5 km s⁻¹ coincides with a second velocity component detected only in the high-resolution spectra map in Sect. B (see also Table B.1), thus we argue that this peak contains a contribution

from an additional velocity component, rather than expansion. HCO⁺ emission towards CygX-N63 is significantly weaker than in the other cores and radiative transfer models show that depletion is strongest in this core. Nevertheless, the HCO⁺ line shows a slight, blue-shifted shoulder, which is also indicative of infall motions. Our best-fit radiative transfer model gives an optically thick line for HCO⁺ with an infall speed of ~ 0.1 km s⁻¹. High depletion, as shown by Rawlings & Yates (2001) based on numerical simulations, might explain this rather weak indication of infall.

5.2.4. Coherent flows seen at high spatial resolution

The high spatial resolution PdBI velocity maps in Fig. 5 (second column of panels) display velocity fields that are similar to those of the purely single-dish data (first column of panels in Fig. 5), particularly in terms of the global rotation-like gradients discussed above in Sect. 5.2.2. On the other hand, these global motions are found to have a more complex morphology on small scales with stronger local gradients, and more importantly with the H¹³CO⁺ line profiles, which are not single Gaussians and clearly divide into several individual velocity components.

These individual components may correspond to coherent features in velocity. To trace the bulk emission from the mass reservoir, we integrate around the rest velocity of each MDC and then separate the emission from the other components by integrating in the blue and the red side of the velocity range. This representation allows us to study the distribution of gas associated with the bulk emission and trace the morphology of the potential coherent velocity features of these individual components.

Figure 8 shows CygX-N3, where the bulk emission at a rest velocity of 15 km s⁻¹ (gray scale) coincides with the main continuum peaks (dashed black contours) and shows an elongated, filamentary structure centered on it, as well as hints of sub-filaments in the north-east and south-west edge, perpendicular to it. The blue and red-shifted spectral components have a bipolar structure indicative of velocity gradients or shears along these sub-filaments. To investigate the velocity structure of these sub-filaments, we show position-velocity cuts along them. The upper cut shows a global smooth shift in velocity, but with hints of two sharp transitions or jumps at offsets of $16''$, $3''$ and $6''$, $10''$. The lower cut shows also a strong red component with a smooth shift in velocity and at ~ 15 km s⁻¹ a sharp change in velocity between offsets $-4''$, $-5''$ and $-5''$, $-4''$. These velocity shears may be similar to the velocity jump revealed in NGC 2264-C by Peretto et al. (2006).

We present spectra across a cut through the sub-filaments. In the upper one, until offset $16''$, $3''$ the blue component dominates and seems to remain at the same velocity, then the spectra suddenly becomes broader peaking at the rest velocity. After $8''$, $9''$, the red component appears and becomes more dominant at $0''$, $15''$, even if the separation between the main and the red component is less clear. The position of the red component is also compatible with a fixed velocity along the sub-filament. The separation between the blue and the bulk emission is ~ 0.75 km s⁻¹ and between the red and the bulk emission is ~ 0.55 km s⁻¹. The lower cut shows both the blue and red spectral components from $-1''$, $-8''$ to $-5''$, $4''$ and a velocity jump from the blue to the main component is seen at $-6''$, $-2''$ offset. It is apparent that the velocity separations are much larger in the lower than in the upper cut up to a total velocity difference of ~ 2.5 km s⁻¹ between the red and the blue component in the lower cut. Towards the continuum peak, the spectral components

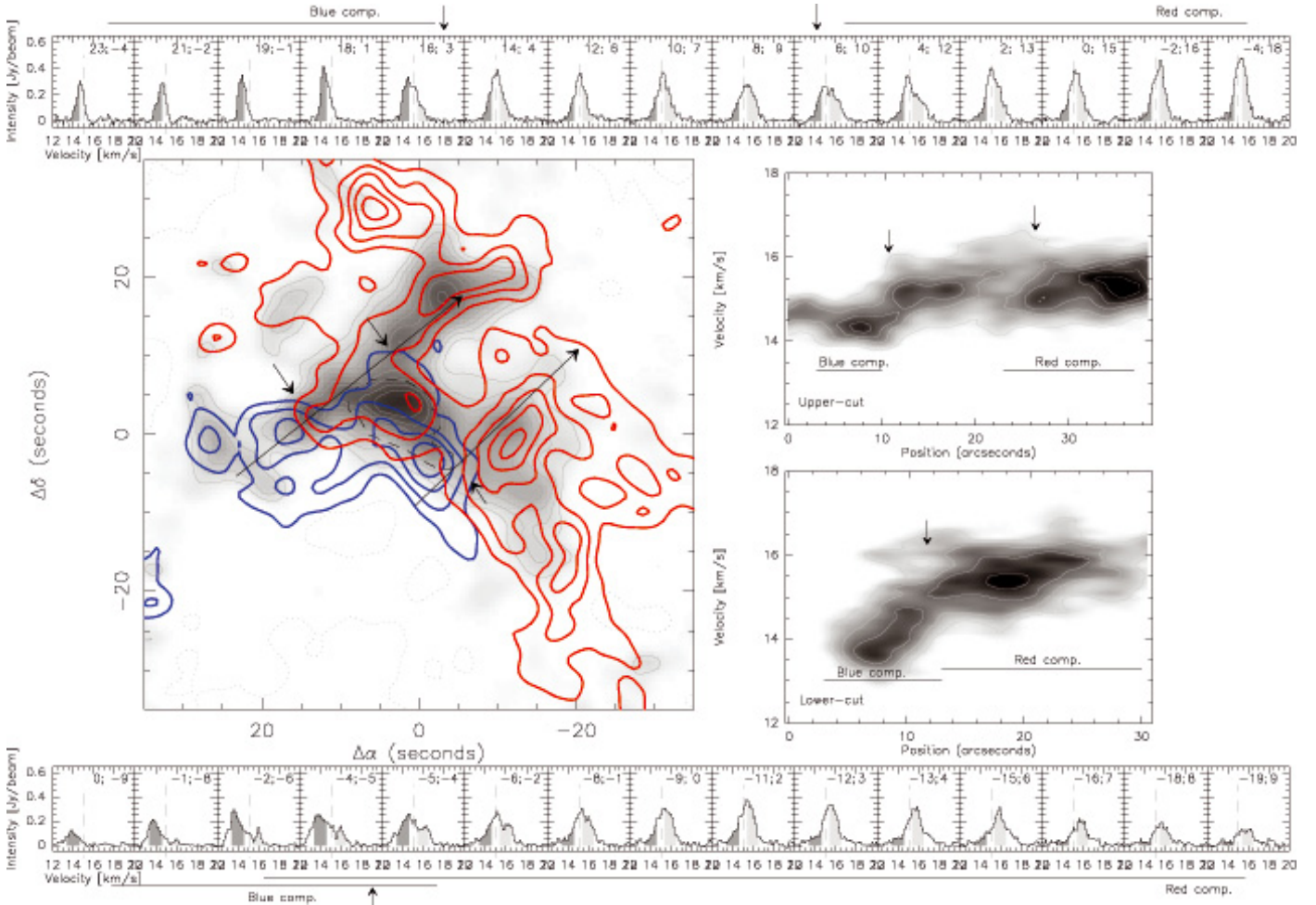


Fig. 8. The left main panel represents the H^{13}CO^+ emission obtained with the PdBI and zero-spacings. The gray scale shows integrated intensity around the v_{lsr} , between $14.5\text{--}15.5\text{ km s}^{-1}$. Blue contours correspond to integrated intensity between $13.5\text{--}14.5\text{ km s}^{-1}$ and red contours show integrated intensity between $15.5\text{--}16.5\text{ km s}^{-1}$. Contours go from $5\times\text{rms}$ noise and increase in steps of $3\times\text{rms}$ noise. For comparison, the black dashed contour shows the 30% of the peak intensity of the 3 mm continuum map. Fully sampled spectra are extracted in two cuts following two filamentary structures indicated by long arrows, where the position corresponding to each spectra are shown in the upper right corner. These cuts are shown in the top and bottom line of the figure. The integration ranges from the blue-shifted component are in dark gray and light gray shows the red component. The v_{lsr} is shown by a dashed gray line. The two plots of the right main panel show position-velocity diagrams for the upper and lower cuts representing the same spectra, respectively. Short arrows indicate the position of velocity jumps seen in the spectra and mark the same positions in the extracted spectra and the position-velocity cuts.

merge into a single, broader line suggesting *physical interaction* between the two components. Summarizing, velocity shifts along organized gas structures are seen but a more careful analysis of the line profiles appears to uncover rather local shears than smooth velocity gradients between the individual velocity components. Interestingly, these velocity jumps correspond to weak continuum sources (see Fig. 11), which may be in an early stage of their formation.

In contrast, CygX-N63 is shown in Fig. 9, where the bulk emission at a rest velocity of -4.3 km s^{-1} is similarly centered close to the continuum peaks and shows hints of a north-west to south-east organized elongated structure. The red and blue shifted emission shows a bipolar structure perpendicular to the main filament. The position-velocity cuts along these structures exhibit however, a far smoother shift in velocity or a weaker velocity shear than in CygX-N3. Cuts of spectra also indicate that the line-profiles are less complex as for CygX-N3 and could be compatible with a single line component, which shows a shift

in velocity of $\pm 0.6\text{ km s}^{-1}$. Altogether, CygX-N63 seems to be more ordered than the example above.

In this systematic way, we find similar trends in the other fields, but owing to a wider range in the complexity of individual velocity components they are less clear for CygX-N12, -N48, and -N53 respectively (see Figs. C.1–C.3 in Appendix C). Cuts of spectra and position-velocity maps are therefore presented centered on the continuum peaks and perpendicular to each other to provide a glimpse of the spatial distribution of the velocity components. Towards CygX-N12, the main component is dominated by spherical extended emission with a large number of individual components and no clear morphology can be found for the blue and red components. As the spectra show, the two components are both visible over a large extent of the map with a velocity of $\sim 14.3\text{ km s}^{-1}$ and $\sim 15.7\text{ km s}^{-1}$. These lines show either a shift in velocity over $\sim \pm 1\text{ km s}^{-1}$ with respect to the systemic velocity of 15.2 km s^{-1} or may be additional components.

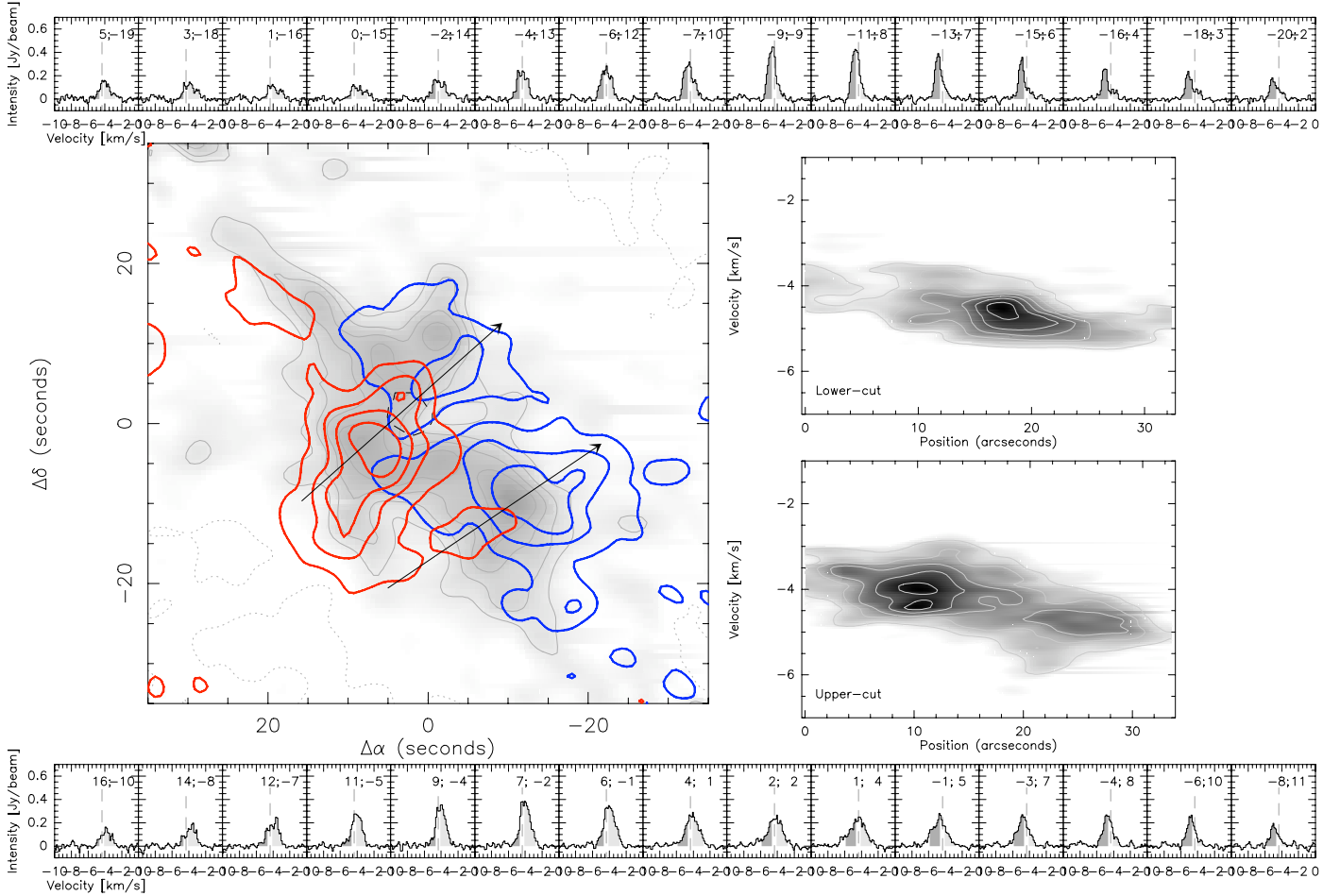


Fig. 9. CygX-N63 presented similarly as Fig. 8. Integration ranges for the gray scale is -4.0 to -4.7 km s^{-1} , red contours are integrated between -2.7 to -4.0 km s^{-1} , blue contours are integrated between -4.7 to -5.7 km s^{-1} . Contour levels go from $5 \times \text{rms}$ noise by steps of $3 \times \text{rms}$ noise.

Similarly, towards CygX-N48 several line components are detected within a velocity range of 6 km s^{-1} corresponding to the most complex dynamics in the sample. Two main components can still be distinguished, one around -5.5 km s^{-1} and one around -3.8 km s^{-1} , both displaying shifts in velocity relative to the rest velocity of the core, and additional components also appear, which is indicative of complex kinematics.

In CygX-N53, the bulk emission at a rest velocity of -4.2 km s^{-1} shows a north-south elongation, although the determination of the rest velocity may be biased by the surrounding large-scale filament, which may have a redder bulk emission. Bipolar blue and red-shifted emission is seen close to the continuum peak, but the tendency is less clear as for CygX-N3.

We conclude that, except perhaps for CygX-N63, all MDCs of the sample display a mixture of several velocity components separated by up to several km s^{-1} , and show drifts and discontinuities in velocity. The spatial distributions of these components suggest that they are associated with the MDCs and indicate that they do not show up as only individual fragments that could be associated with the dust continuum fragments discussed in Paper I. They appear instead as filamentary structures, showing systematic velocity differences leading to local shears. For three of the five MDCs, these velocity features averaged on the scale of the MDC result in a rotation-like motion, and for four of them, there is also an indication of global infall. This is as if the global motions (rotation and infall) split into small-scale individual streams or flows when observed at high spatial

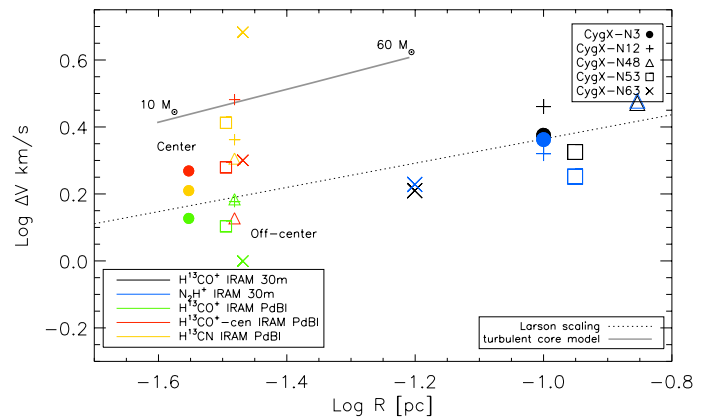


Fig. 10. We plot line-widths of the MDCs taken from single-dish and high angular-resolution data. The corresponding sizes are taken from Motte et al. (2007) for the single-dish data, while for the high angular-resolution data sizes show the synthesized beam of the PdBI. The Larson-scaling is indicated by a dotted line. Gray line indicates the fiducial model of McKee & Tan (2003) with a surface density of ~ 1.7 g cm^{-2} and a final stellar mass of 10 – 60 M_{\odot} . Different colors indicate the different tracers observed with only single-dish or with the interferometer.

resolution (see Sect. 5.5.1 for a further discussion of the nature of these flows).

5.3. Importance of the turbulent support on small scales

A detailed understanding of global organized motions at both low and high angular-resolution is required to recognize the role of support by micro-turbulence on small-scales. In Sect. 5.2.1, we pointed out that turbulence within the MDCs on global scales (~ 0.1 pc) tends to be smaller than required by the turbulent core model. Here we can investigate this trend on smaller scales, where the level of micro-turbulence is traced by the line-dispersion of the individual spectral components recognized in the previous section. Figure 10 shows these results, where the average velocity dispersions of the individual components decrease from ~ 1 km s $^{-1}$ on a ~ 0.1 pc-scale to ~ 0.6 km s $^{-1}$ on a ~ 0.03 pc-scale.

Velocity dispersions towards the central regions (3 mm continuum peaks, indicated by contours in Figs. 8–9) were also extracted. Interestingly, the average velocity dispersion is larger, ~ 0.86 km s $^{-1}$, towards the center than in the off-center positions.

These velocity dispersions are close to the predictions of the McKee & Tan (2003) model. However the line-widths in the central regions might not be representative of the bulk of the central dense material for two reasons. For H 13 CO $^{+}$, the high level of depletion means that only the outskirts are traced, which could have a larger velocity dispersion and H 13 CN may trace only higher temperature gas influenced by stellar feedback (outflow shocks). Alternatively, local turbulent support could be compatible with the McKee & Tan (2003) model on these small scales in the central regions.

On the other hand, we point out that the turbulent line-dispersions of the individual velocity components, which are generally found off-center, are more representative of the pre-collapse gas and are smaller than the model values. They are found to fall on the Larson scaling relation.

5.4. Are massive star-forming cores in equilibrium?

The fundamental question is whether MDCs are in a quasi-static equilibrium or are governed by dynamic processes. In the scenario proposed by McKee & Tan (2003), massive cores should evolve in a quasi-static equilibrium, where a high effective turbulent pressure balances gravity. Once gravity becomes stronger than the effective pressure within the core, the core collapses monolithically to form a single or a binary object. During the quasi-static evolutionary stages, a homogenous medium should develop a central concentration of matter while it is stabilized by its internal micro-turbulence. Comparing our single-dish observations of optically thin emission (H 13 CO $^{+}$), we confirm a centrally peaked distribution of emission in a homogenous medium.

In the sections above, we systematically searched for this support, which can be either micro-turbulence, magnetic fields, or rotation. Without considering magnetic fields, we found that: *a)* line-dispersions on a 0.1 pc-scale tend to show that micro-turbulence alone is insufficient to stabilize MDCs using the turbulent-core model; *b)* line-dispersions on small-scales indicate that the initial conditions may be even less turbulent; *c)* rotation-like ordered bulk-motions are not sufficient either to stabilize MDCs (Sect. 5.2.2). Altogether this gives a coherent view of MDCs being out of equilibrium state, as indicated also by global infall motions and supersonic flows.

5.5. Dynamical processes in the MDCs

5.5.1. Evidence of converging flows

Several indications are found for dynamical processes acting on small-scales. The individual velocity components seen in the high resolution H 13 CO $^{+}$ lines are most clearly understood as individual flows (Sect. 5.2.4). Since the MDCs are probably in global collapse, these flows are expected to stream inward. They should then ultimately interact in the central regions to build up high density cores at the stagnation points, creating the seeds for the protostellar objects. We estimated the crossing times of these convergent flows by dividing the characteristic size of the core (on average $R_{\text{core}} = 0.1$ pc) by the characteristic velocity shift given by the largest separation of the individual spectral components (δv) discussed in Sect. 5.2.4: $\tau_{\text{cross}} = 9.8 \times 10^5 \frac{R_{\text{core}}}{[\text{pc}]} \frac{\delta v^{-1}}{[\text{km s}^{-1}]}$. In Table 5, we list these parameters and indicate the free-fall times (τ_{ff}) from Paper I. For CygX-N63 the crossing time estimate is based on the velocity dispersion of the spectra, since the individual velocity components are less clear. To calculate the crossing times, we adopted a correction for a possible inclination effect assuming an average angle to the line-of-sight of $\sim 57.3^\circ$ (which is the average angle assuming a random distribution of orientation angles). We give also the range of τ_{cross} for variations of the angle by $\sim 20^\circ$ to give a hint of the effect of the inclination uncertainty.

We find that all crossing times are comparable to the free-fall times, which indicates that these flows are the main driver of the evolution of MDCs, and can clearly play a major role in building up the material from which massive protostars form.

The origin of these small-scale flows may just be a natural consequence of the large-scale turbulent nature of the parent clumps and clouds. On pc-scales, Schneider et al. (2010) showed that massive structures, like the DR21 filament itself, can be formed by dynamical processes and converging flows, pointing out that on sub-parsec scales dynamical processes are also important, leading to a complex view of hierarchical dynamics from pc-scale down to the protostar scale.

5.5.2. Importance of competitive accretion

In a broad view of the competitive accretion scenario (Bonnell & Bate 2006), the above discussed high level of dynamics necessary leads to competition for mass between the protostars. Even if these small-scale flows converging to the central parts of MDCs were revealed in the previous sections, it remains unclear whether these flows continue to build up the mass reservoirs of the protostars. The timescale for a new prestellar/protostellar seed to form by convergent flows is given by the typical velocity shears observed in the most dynamical regions of the MDCs on a scale of the separation between the protostars (~ 5000 AU in Paper I). The largest velocity shifts observed over this projected distance are ~ 3 km s $^{-1}$, which imply a typical timescale of $\sim 10^4$ yr, a factor of a few smaller than the crossing time on the scale of the MDCs. This means that during a crossing time of the MDCs, several protostars could form by the convergence of several small-scale flows. This timescale of $\sim 10^4$ yr is also only slightly longer than the typical free-fall time derived for the continuum fragments reported in Paper I (on average of 4000 yr). If the protostellar cores collapse on a few free-fall times as in low-mass star-forming regions, the formation timescale may be of the same order of magnitude than the collapsing time, and the mass input from flows during collapse can be significant. This

Table 5. Kinematic parameters corresponding to the identified flows.

Source	δv [km s ⁻¹]	τ_{cross} ×10 ⁴ [yr]	τ_{ff} ×10 ⁴ [yr]
CygX-N3	2.5	2.4–3.8	6.0
CygX-N12	3	2.0–3.2	5.9
CygX-N48	3.5	1.7–2.7	6.1
CygX-N53	1.1	5.4–8.7	7.6
CygX-N63	0.5	11.8–19.1	3.4

Notes. The velocity difference indicates the relative velocity of the flows on the global scale of the MDCs, which was used to calculate the crossing timescales.

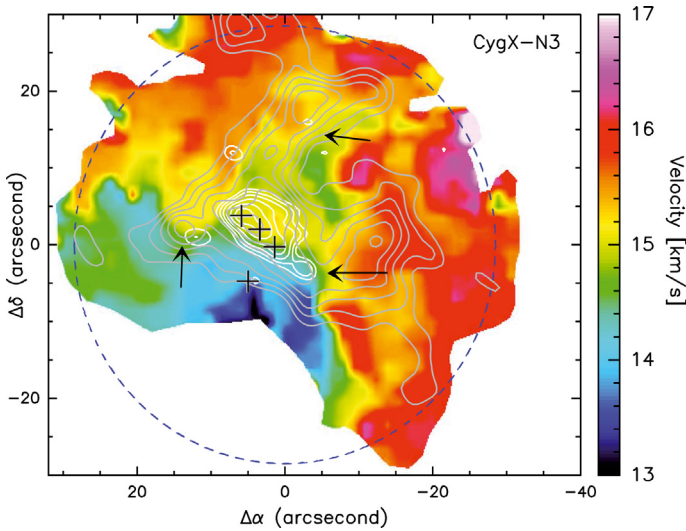


Fig. 11. The velocity field obtained from IRAM 30 m+PdBI H¹³CO⁺ data (in the same way as for Fig. 5b towards CygX-N3 is shown with overlays of integrated intensity (contour levels are from 20σ to 50σ in steps of 5σ. White contours show the 3 mm continuum emission. Arrows indicate the shears associated with weak continuum emission.

therefore implies that there may be a significant amount of competitive accretion in the MDCs of Cygnus X.

5.5.3. Origin of the diversity between the 5 MDCs

From the fragmentation properties (Paper I) and a kinematical point of view (this work), our sample of MDCs is diverse. This diversity can reflect either the different evolutionary stages or the different initial conditions of the MDCs.

In CygX-N12, -N53, and -N63, the gravitational potential is dominated by a few but massive fragments at the center, corresponding to more than 30% of the total mass. In these cases, the self-gravity of the MDC is dominated by these few fragments, which are then able to collect most of the remaining flowing mass if the convergent flows remain active. In CygX-N3 and -N48, on the other hand, the mass in the already formed fragments is a smaller fraction of the total mass, therefore the local gravitational field is not dominated by the observed fragments, but more by the self-gravity of the mass reservoir of the MDC. These MDCs are either intrinsically different from CygX-N12, -N53, and -N63 or they are younger and will evolve to similar MDCs dominated by a few massive fragments. The high resolution velocity field in H¹³CO⁺ should indicate whether or not the fragments are still collecting mass from their parent MDCs, and

therefore may help us to discriminate between the two possibilities.

In CygX-N3, the three most massive fragments are located on a significant shear in velocity, which indicates that they can still gain mass from the MDC reservoir. At the same time, three shears associated with significant H¹³CO⁺ emission peaks are also visible and could therefore correspond to newly forming protostars (all three correspond also to weak continuum peaks as indicated by arrows in Fig. 11). The relative intensity of the shears and associated H¹³CO⁺ peaks suggest that a large number of protostellar seeds collect mass from the MDC mass-reservoir leading to the formation of a whole cluster of protostars.

In CygX-N12, the existence of several velocity components implies that the kinematics is complex. Since about 70% of the total mass of the MDC is still available, there is a potential for CygX-N12 to evolve towards a state similar to CygX-N53 with two main massive fragments in the central regions.

In CygX-N48, the observed shears are intense and are located in the central regions close to but not necessary exactly associated with the main central fragments. It is as if the first fragments are not yet clearly decoupled in the central, very active region. This is therefore a good candidate MDC to be in an early phase of evolution, perhaps leading later on to a MDC similar to CygX-N53.

In CygX-N53, most of the total mass is contained in two main, central fragments. No clear shears are observed in the central regions. Some indications of shears are seen in the southwest outskirts of the MDCs, though they are less convincingly associated with the MDC (this MDC is located in the northern part of the massive DR21 filament). This MDC therefore probably evolves with there being no significant flowing gas present in the central regions.

Finally, CygX-N63 is a special case with only one central peak of emission in the continuum as if it were not sub-fragmented, and with a global collapse towards this single object. The kinematics displays a rotation-like gradient, which may correspond to a large-scale shear, revealing that the object still collects mass. Interestingly, besides this smooth shift or a weak shear seen towards the main continuum emission, a small-scale shear is observed in the south-west edge of the field coinciding with weak 3 mm continuum emission, which could lead to the formation of a new protostar.

We have therefore three MDCs (CygX-N12, N53, N48), which could correspond to three cores of similar nature seen at three different evolutionary stages: CygX-N48 corresponding to a younger and CygX-N53 to a more evolved phase. CygX-N3 seems to be forming a cluster of at least six protostars with the total mass being shared between them without any dominating massive one. Finally, CygX-N63 can be regarded as a special case: a single collapsing object that does not display strong dynamics in a collapsing, large-scale envelope. Alternatively, it can be seen as the extreme case of the massive star forming MDCs discussed here (CygX-N12, N53, and N48) with only one protostar dominating the collapse. We therefore propose that the initial conditions may explain the differences between CygX-N3, CygX-N12/N48/N53, and CygX-N63, while the evolutionary state would be the explanation of the observed differences between CygX-N12, N48, and N53.

6. Summary and conclusions

We have presented a detailed study of high-density gas tracers towards 5 MDCs in Cygnus-X focusing on their kinematic

properties on global (~ 0.1 pc) and small scales (~ 0.03 pc). Our main findings are:

1. On ~ 0.1 -pc-scales, dense gas traced by H^{13}CO^+ and HCO^+ exhibit infall signatures in CygX-N12, -N48, -N53, and -N63. The velocity fields indicate coherent, organized bulk motions towards CygX-N3, -N53, and -N63 with a rotation-like pattern, while towards CygX-N12 and -N48 no global velocity gradients are dominant.
2. Simultaneous radiative-transfer modeling of H^{13}CO^+ and HCO^+ indicates that because of depletion effects the emission is a more accurate tracer of the bulk of material around the protostars ($\sim 10^5$ – 10^6 cm^{-3}). Depletion is found to be most significant in CygX-N63.
3. At high angular-resolution, we find a better correspondence of H^{13}CN with continuum peaks than H^{13}CO^+ .
4. High angular-resolution maps with the PdBI in H^{13}CO^+ reveal significant substructure on small-scales and in all MDCs several line components are found, which can be distinguished into small-scale coherent flows with intrinsic velocity gradients and shears.
5. An analysis of the line-dispersion of the high-angular resolution H^{13}CO^+ spectra has questioned whether the level of micro-turbulence on small-scales is enough to provide sufficient support against gravitational collapse.
6. At high angular-resolution, the larger-scale global coherent motions are resolved into individual coherent flows with filamentary structures, showing velocity shifts and more importantly shears/discontinuity in velocity towards the continuum peaks. The relative difference in the velocity positions of the flows give dynamical timescales of the order of the free-fall timescale for CygX-N3, -N12, -N48, and -N53. Only for CygX-N63 do we find order-of-magnitude longer dynamical timescales.
7. Small-scale velocity shears may indicate $\sim 10^4$ yr dynamical timescales for new protostellar seeds built-up by small-scale converging flows.
8. The fragmentation and the kinematic properties of our sample imply that CygX-N48, -N12, and -N53 may be in different evolutionary stages, while different initial conditions may explain the differences between CygX-N3 and -N63.

Acknowledgements. The authors would like to thank the anonymous referee for its critical review of the article and for the useful comments and suggestions which have lead to a significant improvement of the text. The authors also wish to thank to V. Ossenkopf for providing the latest version of *Simline*. T. Csengeri acknowledges support from the FP6 Marie-Curie Research Training Network Constellation: the origin of stellar masses (MRTN-CT-2006-035890). Part of this work was supported by the ANR (Agence Nationale pour la Recherche) project PROBeS, number ANR-08-BLAN-0241 (LA).

Appendix A: Details on radiative transfer modeling

To model the molecular line emission of MDCs, we consider a core embedded in its parent molecular clump and a smooth transition between the physical parameters. For each core, we used a simple model with the same assumptions: the mass and the radius were taken from continuum data of Motte et al. (2007) and the corresponding 90% mass and radius were used to constrain the density profile with a power-law exponent of $\alpha_1 \sim -2$ (as done in Schneider et al. 2010). The NH_3 measurements of Wiene (2008) were used to constrain the temperature and the size of the NH_3 cores that corresponds to the measured temperature. Using these parameters to obtain a mass-averaged temperature within a size slightly larger than the size of the MDCs (~ 0.2 pc), the temperature profile was then constrained. The

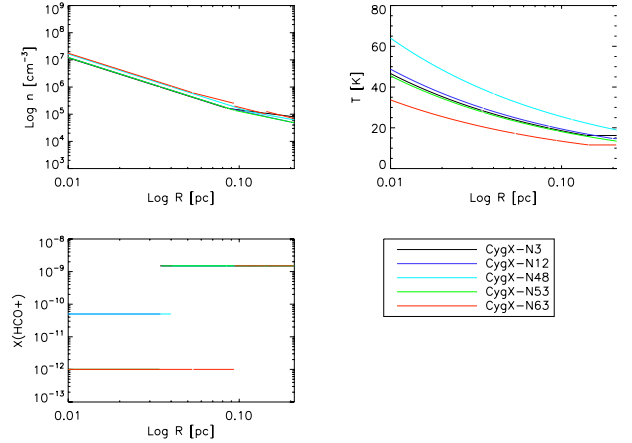


Fig. A.1. Profiles of density, temperature and HCO^+ abundance. Colors indicate the different MDCs.

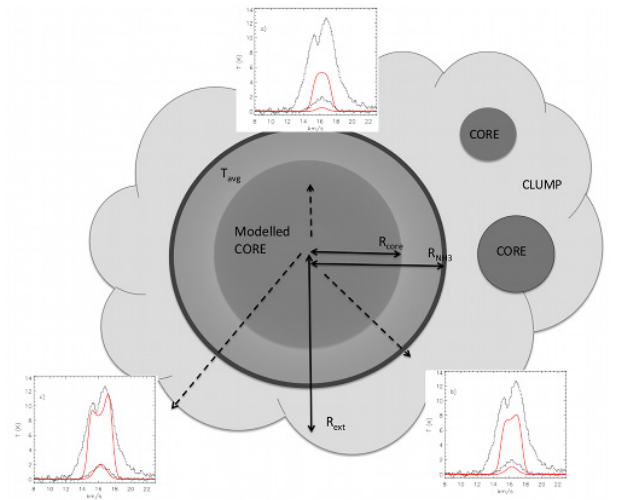


Fig. A.2. The scheme of the physical model. Model spectra are produced for CygX-N3 in three variations, **a)** modeling only the core, **b)** the core corresponding to the NH_3 measurements, **c)** modeling the core and its embedding clump.

cores were embedded in a larger structure, a molecular clump (~ 0.3 – 0.6 pc), whose parameters were taken from Motte et al. (2007). We assumed that the size of the clump equaled the outer radius and constrained the density profile with a shallower exponent ($\alpha_2 \sim -1.0$ to -1.6). First estimates of turbulent widths were taken from the Gaussian line-fitting of the H^{13}CO^+ lines. Fig. A.1 shows the density, temperature, and abundance profiles used for the models.

We used an abundance of $X(\text{HCO}^+) \sim 10^{-9}$ (e.g. Hogerheijde & Sandell 2000) and introduce depletion at a given density. We varied both the density at which depletion occurs (10^5 – 10^6 cm^{-3}) and the level of depletion (0–1000). We kept the depletion density and the depletion factor as free parameters and constrained the best fit using all the spectra extracted along the radius (see the results in Figs. A.3–A.7). Thus by fitting a radial profile, we restricted the degeneracy of the model. The explored parameter-space is the same for each MDC and the best fit is determined by comparing the reduced χ^2 values of the fit. From this modeling, we obtained the opacity (τ) and the density where depletion occurs.

Figure A.2 shows a sketch of the model, the core embedded in a clump and the models of the spectra we get at certain radii.

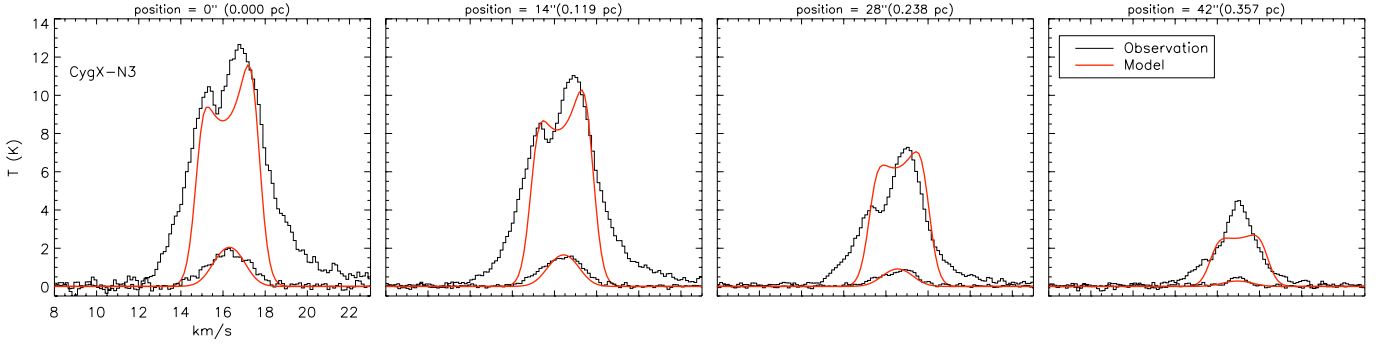


Fig. A.3. HCO^+ and H^{13}CO^+ mean spectra computed over concentric annuli in steps of $14''$ with respect to the map center towards CygX-N3. The black line shows the observations, the red line corresponds to the model.

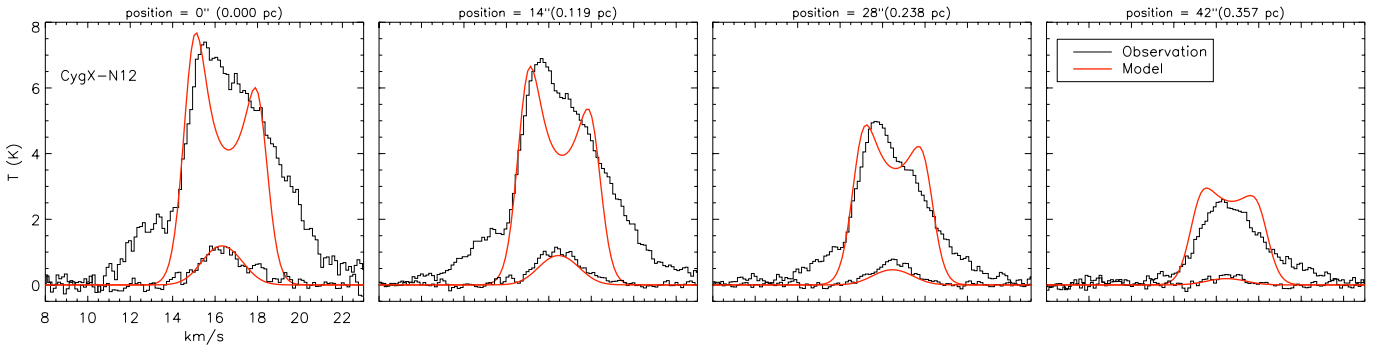


Fig. A.4. Same as Fig. A.3 for CygX-N12.

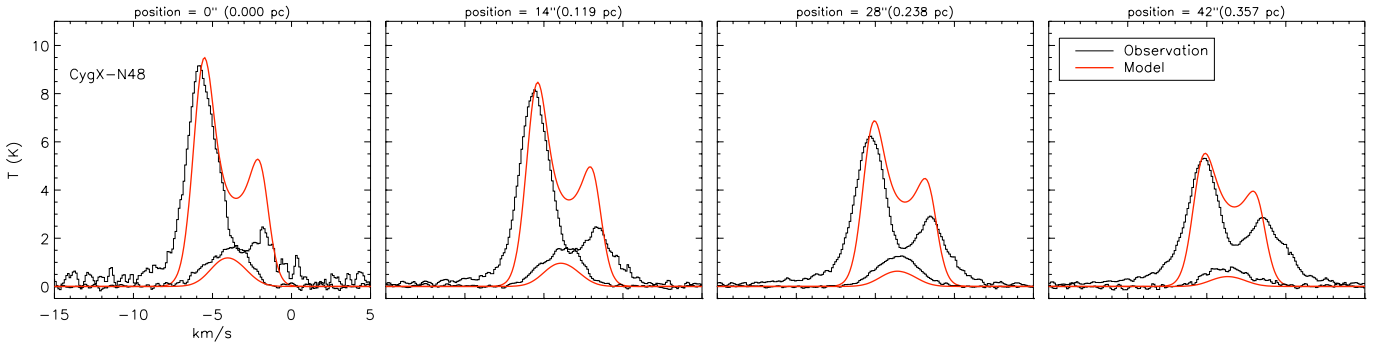


Fig. A.5. Same as Fig. A.3 for CygX-N48.

This shows the emission coming only from the core (a), then within the radius, where NH_3 observations were taken (b) and finally the spectra taken through the whole clump (c) illustrating that a significant part of the emission originate in regions of 10^4 – 10^6 cm^{-3} densities. Figure A.1 shows the obtained density, temperature, and abundance profiles, respectively.

CygX-N3 The HCO^+ spectra show red-shifted asymmetry in the line profiles, which may be an indication of expanding gas. Broad line-wings are present because of the outflowing gas, which we do not aim to reproduce in our model. We confirm with *Simline* that HCO^+ is optically thick and obtain a reasonably good fit with an expansion velocity of $\sim 0.3 \text{ km s}^{-1}$ to the central spectra. The radial fitting of the profile is less good indicating that we either overestimate the optical thickness of the line, or the expansion velocity is not constant. The spectral decomposition shows a second line component at the same velocity of the red-shifted peak, which may indicate, that expansion is not necessarily the reason for the line profile, but an optically

thin second component at the same velocity may also produce a similar line profile. Nevertheless, it is beyond the scope of this work to perform such a detailed modeling.

CygX-N12 Indications of the contributions of more than one line-component can be seen in the spectra of CygX-N12, in addition to broad line-wings, which limits our approach to performing a good modeling of this core. Nevertheless, our results reproduce the line ratio of HCO^+ to H^{13}CO^+ . We note, that the spectra display a shallower shoulder on the red part, which may be an indication of infalling material. Therefore we include 0.2 km s^{-1} as an infall velocity in the model.

CygX-N48 and -N53 The clump associated with both CygX-N48 and CygX-N53 was modeled in detail by Schneider et al. (2010). Here we used the same physical model for all the MDCs, which we adapted to model more precisely the cores embedded within the clump, that has not been considered in Schneider et al. (2010).

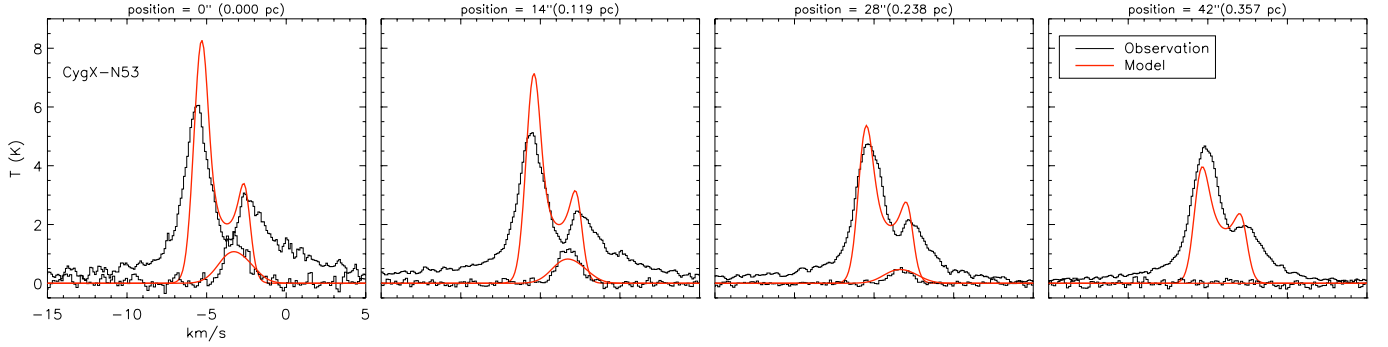


Fig. A.6. Same as Fig. A.3 for CygX-N53.

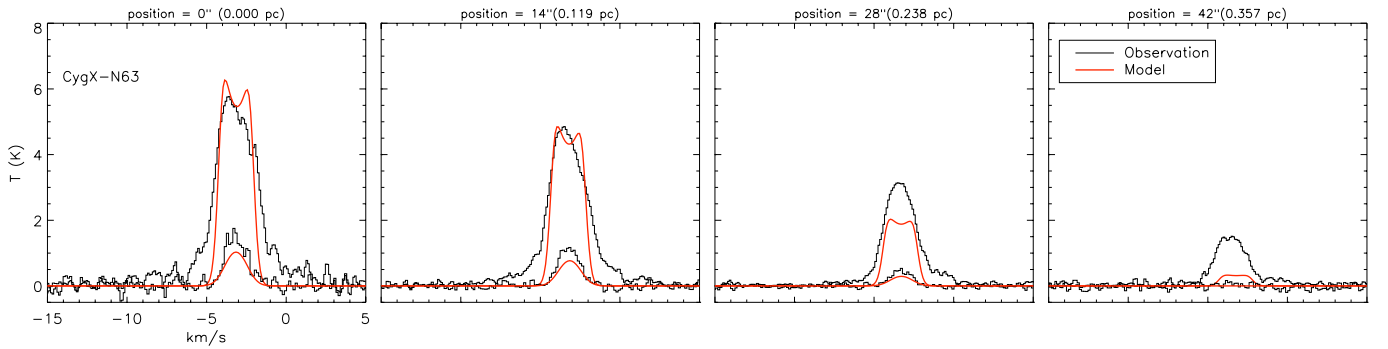


Fig. A.7. Same as Fig. A.3 for CygX-N63.

CygX-N63 CygX-N63 has the weakest HCO^+ and H^{13}CO^+ emission of all the MDCs and the morphology of its high-resolution emission confirms that there is a hole centered on its continuum peak. Our best-fit model infers a high depletion factor and a lower depletion density ($\sim 2 \times 10^5 \text{ cm}^{-3}$) than in the other MDCs. We note that the line-profile is similar to that of CygX-N12, a shallow red shoulder of the spectra may be indicative of slight infall-motions that we model with a 0.1 km s^{-1} infall velocity.

Appendix B: Decomposition of spectral line components in H^{13}CO^+

To distinguish the individual components seen in the spectral line maps (Fig. 2b), a double Gaussian fit was performed for all spectra with an IDL routine using *MPFIT*. Figure B.1 shows the resulting two-component fits in green and red. We recall that the noise towards the edge of the map is larger. Individual components are fitted across a fixed velocity range with respect to the v_{lsr} . A line is fitted when the signal-to-noise ratio (S/N) exceeds 5, otherwise no second component is fitted. For CygX-N3, -N53, and -N63, the components can be most clearly separated in the outer parts of the core, while in the central part only a single Gaussian is fitted. In the core of CygX-N63, most of the spectra are dominated by one strong component. This tendency is also consistent with the assumption that the double-peaked line-profiles are not due to an opacity effect (thus to self-absorption), because one would expect this to be significant in the positions of the strongest emission associated with the central parts, which is clearly not the case. For CygX-N12 and -N48, the routine clearly identifies the two components across the whole field. We note that the line-positions of CygX-N48 correspond well to the position of the two components seen in H^{13}CN (within $\pm 0.3 \text{ km s}^{-1}$).

Table B.1. Result of spectral decomposition of IRAM 30 m+PdBI H^{13}CO^+ lines.

Source	peak velocity (v_{lsr})		line-dispersion (σ)	
	1st comp. [km s^{-1}]	2nd comp. [km s^{-1}]	1st comp. [km s^{-1}]	2nd comp. [km s^{-1}]
CygX-N3	15.33	16.75	0.56	0.58
CygX-N12	15.36	16.87	0.6	0.68
CygX-N48	-4.46	-2.75	0.65	0.65
CygX-N53	-4.43	-3.17	0.55	0.54
CygX-N63	-4.39	-2.89	0.49	0.36

We summarized the fit parameters in Table B.1. The identified components in the spectra correspond to an average (where the S/N exceeds 5), since they are not fixed in position but display systematic shifts in velocity.

Appendix C: Coherent flows seen at high spatial resolution – continued

CygX-N12 displays several velocity components in its spectra. As mentioned in Sect. 5.2.4, because of their complexity it is not possible to determine their spatial structure in our systematic approach. Position-velocity cuts indicate a complex mixture of several line components and the extracted spectral profile confirms this complexity. Individual velocity components appear across a range of $\sim 2.5\text{--}3.5 \text{ km s}^{-1}$.

CygX-N48 shows a similarly complex mixture of individual velocity components with the individual components being separated across a range of $\sim 3.5 \text{ km s}^{-1}$.

CygX-N53 may have a similar configuration as CygX-N3, but the separation of the individual components and thus the location of velocity shears is less clear.

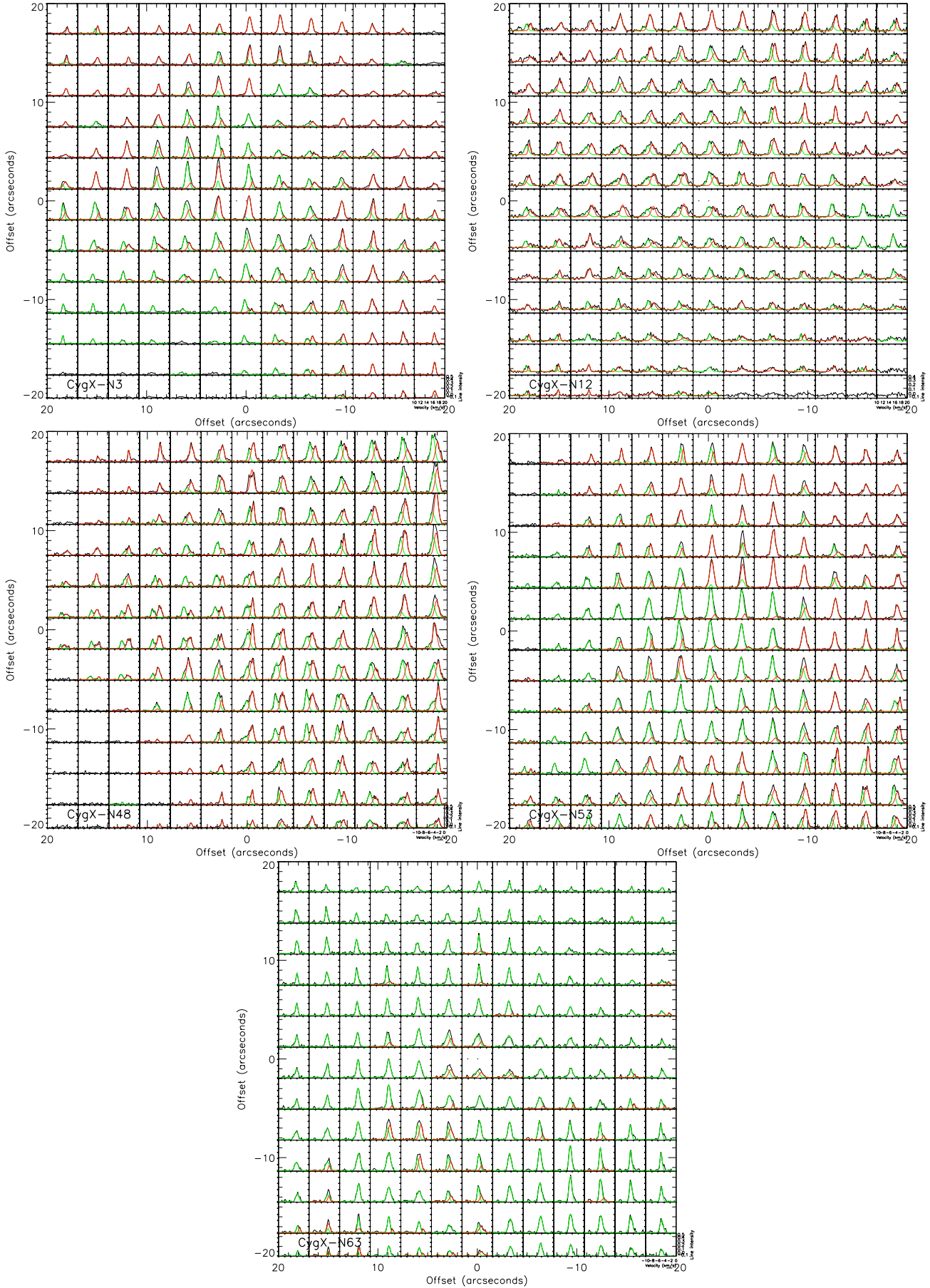


Fig. B.1. Spectral decomposition of the line-components seen in 30 m+PdBI H^{13}CO^+ spectra maps. Black line shows the observed spectra, while red and green lines show the resulting fits of two components. We show only the components with a $S/N > 5$.

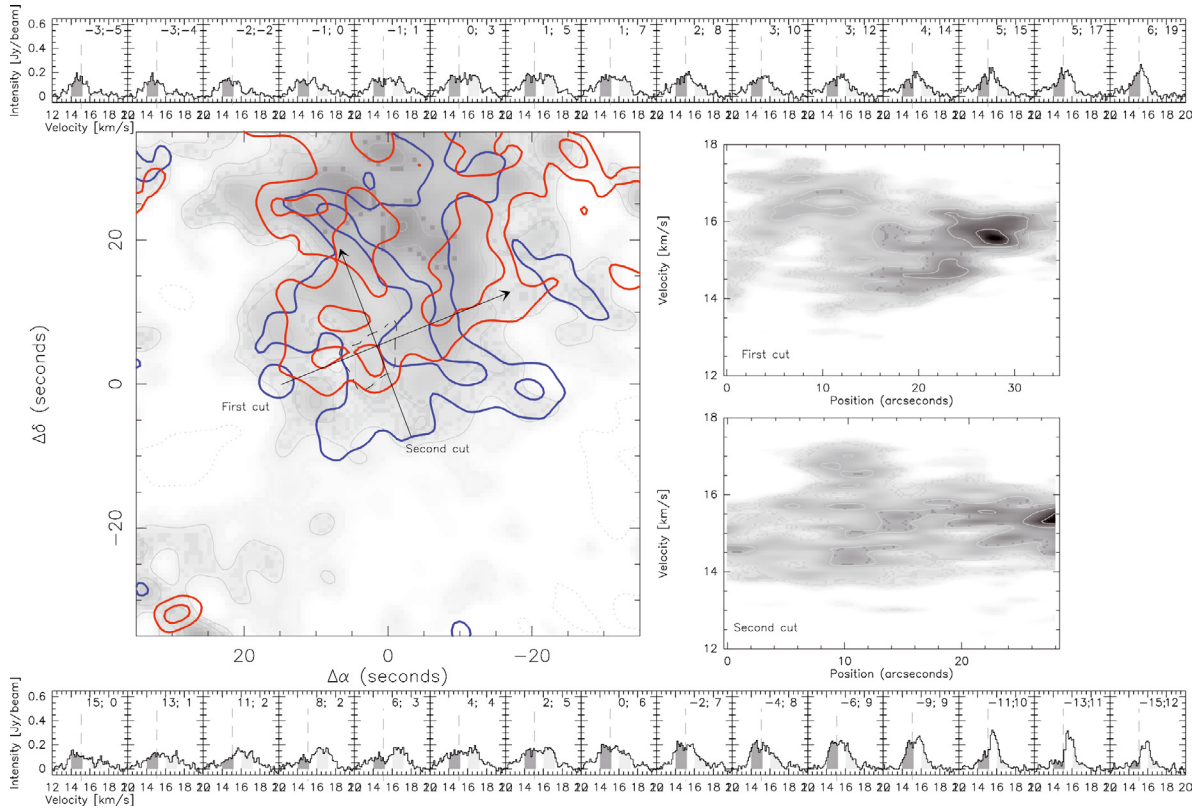


Fig. C.1. CygX-N12 presented as in Fig. 8. Integration range for the gray scale is 15.1 to 16.1 km s⁻¹, red contours show an integration range between 16.1 and 17.1 km s⁻¹, blue contours are integrated between 14.1 and 15.1 km s⁻¹. Contour levels go from 5 × rms noise in steps of 3 × rms noise.

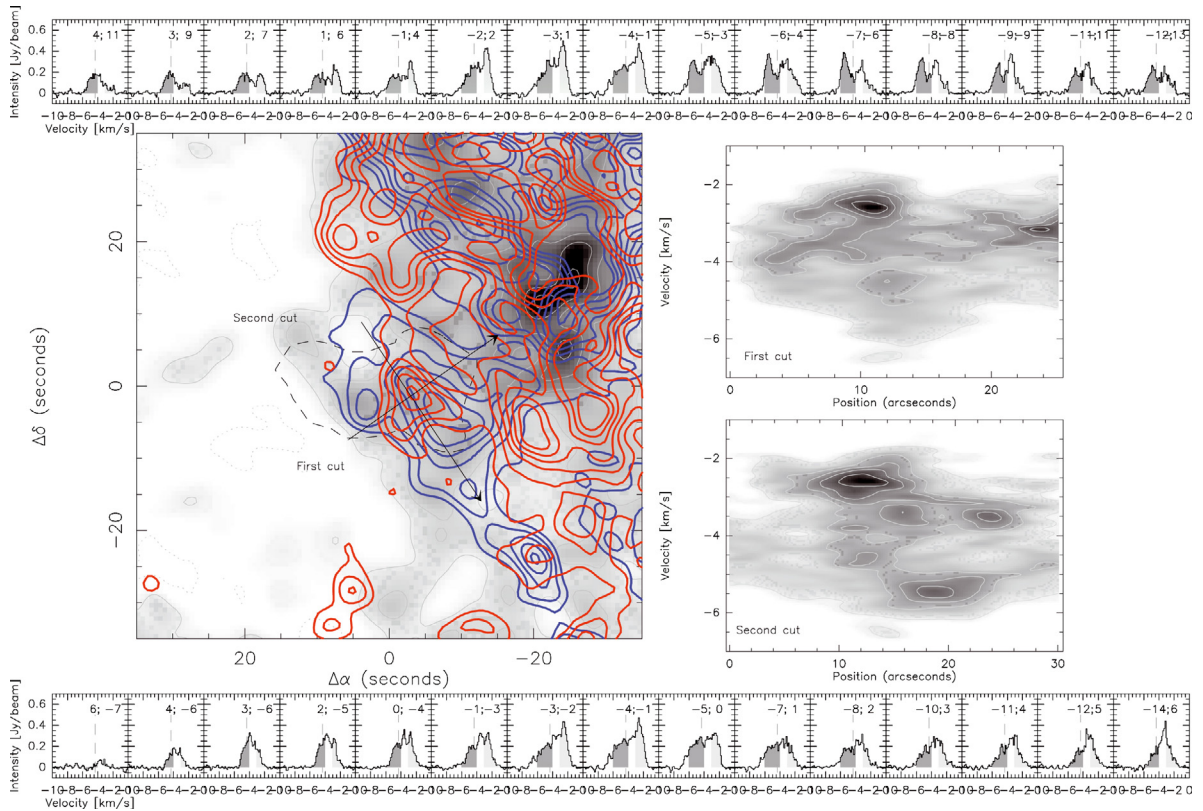


Fig. C.2. CygX-N48 as in Fig. 8. Integration range for the gray scale is -4 to -3 km s⁻¹, red contours show an integration range between -3 and -1 km s⁻¹, blue contours are integrated between -6 and -4 km s⁻¹. Contour levels go from 10 × rms noise in steps of 3 × rms noise.

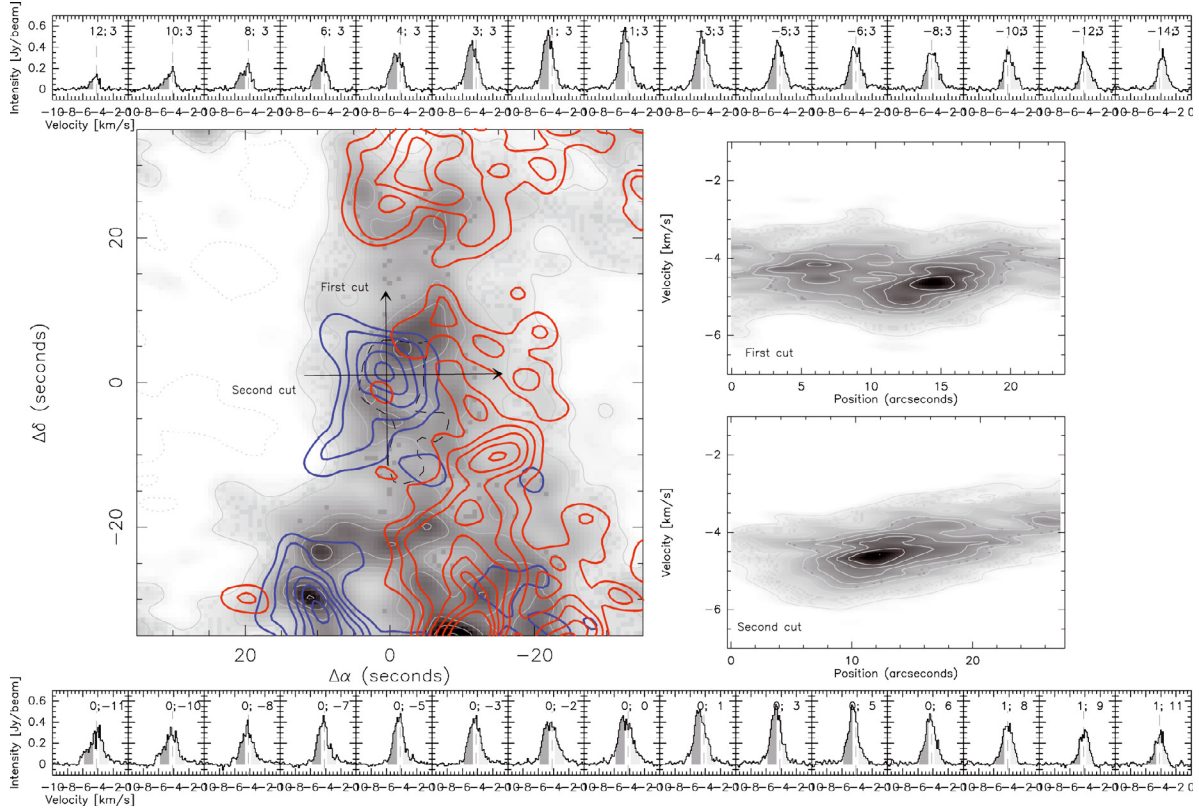


Fig. C.3. CygX-N53 as in Fig. 8. Integration range for the gray scale is -4.7 to -3.7 km s^{-1} , red contours show an integration range between -3.7 and -2.7 km s^{-1} , blue contours are integrated between -5.7 and -4.7 km s^{-1} . Contour levels go from $10 \times \text{rms}$ noise in steps of $3 \times \text{rms}$ noise.

References

- Beltrán, M. T., Cesaroni, R., Neri, R., et al. 2004, *ApJ*, 601, L187
 Bergin, E. A., & Tafalla, M. 2007, *ARA&A*, 45, 339
 Bonnell, I. A., & Bate, M. R. 2006, *MNRAS*, 370, 488
 Bonnell, I. A., Bate, M. R., Clarke, C. J., & Pringle, J. E. 2001, *MNRAS*, 323, 785
 Bonnell, I. A., Larson, R. B., & Zinnecker, H. 2007, in *Protostars and Planets V*, ed. B. Reipurth, D. Jewitt, & K. Keil, 149
 Bontemps, S., Motte, F., Csengeri, T., & Schneider, N. 2010, *A&A*, 524, A18 (Paper I)
 Burkert, A., & Bodenheimer, P. 2000, *ApJ*, 543, 822
 Caselli, P., & Myers, P. C. 1995, *ApJ*, 446, 665
 Caselli, P., Walmsley, C. M., Zucconi, A., et al. 2002, *ApJ*, 565, 331
 Cesaroni, R. 2005, *Ap&SS*, 295, 5
 Chandler, C. J., Gear, W. K., & Chini, R. 1993, *MNRAS*, 260, 337
 Dib, S., Kim, J., Vázquez-Semadeni, E., Burkert, A., & Shadmehri, M. 2007, *ApJ*, 661, 262
 Dib, S., Hennebelle, P., Pineda, J. E., et al. 2010a, *ApJ*, 723, 425
 Dib, S., Shadmehri, M., Padoan, P., et al. 2010b, *MNRAS*, 405
 Downes, D., & Rinehart, R. 1966, *ApJ*, 144, 937
 Fallscheer, C., Beuther, H., Zhang, Q., Keto, E., & Sridharan, T. K. 2009, *A&A*, 504, 127
 Goodman, A. A., Benson, P. J., Fuller, G. A., & Myers, P. C. 1993, *ApJ*, 406, 528
 Guilloteau, S., & Baudry, A. 1981, *A&A*, 97, 213
 Hennebelle, P., & Chabrier, G. 2008, *ApJ*, 684, 395
 Hennebelle, P., & Teyssier, R. 2008, *A&A*, 477, 25
 Hogerheijde, M. R., & Sandell, G. 2000, *ApJ*, 534, 880
 Hora, J. L., Bontemps, S., Megeath, S. T., et al. 2009, *BAAS*, 41, 498
 Jørgensen, J. K., Hogerheijde, M. R., van Dishoeck, E. F., Blake, G. A., & Schöier, F. L. 2004, *A&A*, 413, 993
 Klessen, R. S., & Hennebelle, P. 2010, *A&A*, 520, A17
 Klessen, R. S., Ballesteros-Paredes, J., Vázquez-Semadeni, E., & Durán-Rojas, C. 2005, *ApJ*, 620, 786
 Lada, C. J., & Lada, E. A. 2003, *ARA&A*, 41, 57
 Larson, R. B. 1981, *MNRAS*, 194, 809
 Le Duigou, J., & Knödseder, J. 2002, *A&A*, 392, 869
 Lee, J., Bergin, E. A., & Evans, II, N. J. 2004, *ApJ*, 617, 360
 Mac Low, M., & Klessen, R. S. 2004, *Rev. Mod. Phys.*, 76, 125
 Mac Low, M., Klessen, R. S., Burkert, A., & Smith, M. D. 1998, *Phys. Rev. Lett.*, 80, 2754
 Matzner, C. D., & McKee, C. F. 2000, *ApJ*, 545, 364
 McKee, C. F. 1989, *ApJ*, 345, 782
 McKee, C. F. 1999, in *The Origin of Stars and Planetary Systems*, ed. C. J. Lada, & N. D. Kylafis, NATO ASIC Proc., 540, 29
 McKee, C. F., & Ostriker, E. C. 2007, *ARA&A*, 45, 565
 McKee, C. F., & Tan, J. C. 2002, *Nature*, 416, 59
 McKee, C. F., & Tan, J. C. 2003, *ApJ*, 585, 850
 Motte, F., Bontemps, S., Schilke, P., et al. 2007, *A&A*, 476, 1243
 Mouschovias, T. C., & Ciolek, G. E. 1999, in *The Origin of Stars and Planetary Systems*, ed. C. J. Lada, & N. D. Kylafis, NATO ASIC Proc., 540, 305
 Mouschovias, T. C., & Spitzer, Jr., L. 1976, *ApJ*, 210, 326
 Myers, P. C., Mardones, D., Tafalla, M., Williams, J. P., & Wilner, D. J. 1996, *ApJ*, 465, L133
 Norman, C., & Silk, J. 1980, *ApJ*, 238, 158
 Ossenkopf, V., Trojan, C., & Stutzki, J. 2001, *A&A*, 378, 608
 Padoan, P., & Nordlund, Å. 1999, *ApJ*, 526, 279
 Padoan, P., Juvela, M., Goodman, A. A., & Nordlund, Å. 2001, *ApJ*, 553, 227
 Peretto, N., André, P., & Belloche, A. 2006, *A&A*, 445, 979
 Plume, R., Jaffe, D. T., Evans, II, N. J., Martin-Pintado, J., & Gomez-Gonzalez, J. 1997, *ApJ*, 476, 730
 Rawlings, J. M. C., & Yates, J. A. 2001, *MNRAS*, 326, 1423
 Saito, M., Kawabe, R., Kitamura, Y., & Sunada, K. 2001, *ApJ*, 547, 840
 Schneider, N., Bontemps, S., Simon, R., et al. 2006, *A&A*, 458, 855
 Schneider, N., Csengeri, T., Bontemps, S., et al. 2010, *A&A*, 520, A49
 Shu, F. H., Adams, F. C., & Lizano, S. 1987, *ARA&A*, 25, 23
 Sohn, J., Lee, C. W., Park, Y., et al. 2007, *ApJ*, 664, 928
 Tafalla, M., Myers, P. C., Caselli, P., Walmsley, C. M., & Comito, C. 2002, *ApJ*, 569, 815
 Vázquez-Semadeni, E., Shadmehri, M., & Ballesteros-Paredes, J. 2002, unpublished [arXiv:astro-ph/0208245]
 Vázquez-Semadeni, E., Gómez, G. C., Jappsen, A. K., et al. 2007, *ApJ*, 657, 870
 Wien, M. 2008, *Untersuchung von Ammoniak in massereichen, staubselektierten Sternentstehungsgebieten* (Diplom Thesis)